Chapter 8. First Order Numerical Models of Remedial Ground Densification Techniques

8.1 Introduction

In the previous chapter, simple calculations were presented comparing the total mechanical energy required to treat a unit volume of soil by vibrocompaction, deep dynamic densification, and explosive compaction. However, these calculations did not provide any information on the how the imparted energy is spatially dissipated in the soil. Such information is needed to make comparisons between the dissipated energy required to induce liquefaction during remedial ground densification and during earthquakes, which leads to the focus of this chapter: the development of first order numerical models for computing the spatial distribution of the energy dissipated in the soil during treatment. The proposed models are relatively simple and require a spreadsheet, or other general math program, for implementation; Mathcad 8 (MathSoft, Inc. 1998) was used by the author.

In conjunction with the energy-based earthquake *Capacity* curve, the proposed models are used to predict the spatial extent of liquefaction induced in simple profiles during treatment. Based on the hypothesis that liquefaction is a requisite for the densification of saturated sands, the predicted extent of liquefaction using the proposed numerical models are compared with the spatial extent of improvement predicted using the empirical expressions and guidelines presented in Chapter 7. The purpose of the comparisons, and the ultimate goal of this thesis, is to assess the applicability of using the energy-based *Capacity* curve derived from earthquake case histories in remedial ground densification design.

Before the proposed models are outlined for each of the remedial densification techniques, a brief discussion is presented on the verification and validation of numerical models.

8.2 Numerical Model Verification and Validation

The term "numerical model" refers to the mathematical representation of a physical system or process. Numerical modeling techniques range in sophistication and complexity. In general, simpler models (or lower order models) require a greater understanding of the system or process being represented, while more sophisticated models (or higher order models) require a greater understanding of the specific modeling technique being employed (e.g., finite element method). A good philosophy is to start simple and progressively use more sophisticated models until a comfort level is reached that the actual system or process is being adequately represented. In doing so, the results from lower order models are used to check the appropriateness of the specifics of the higher order models (e.g., type of elements used, boundary conditions, constitutive equations), and the higher order models are used to check the appropriateness simplifying assumptions and the inherent limitations of the lower order models. Only after the results from the lower and higher order models are reconciled, and most importantly, only after the computed results are favorably compared with observations from well-documented field case histories, can any confidence be placed in the appropriateness of the models.

Alternatively to the above approach, simple models are often evaluated by direct comparisons with field observations, without the benefit of comparisons with higher order model predictions. For processes for which an abundant amount of well-documented field case histories are available, thorough evaluations of the simple models can be performed by this approach. However, for processes for which limited field case histories are available, this evaluation approach should be used with caution. First, if field observations are only available for complex profiles, unfavorable comparisons between predicted and observed results may lead to the model being summarily labeled inaccurate, when in actuality, the model may be suitable for analyses of less complex profiles. Second, if field observations are available for simple profiles, favorable comparisons between predicted and observed results may lead to over confidence in the predictive capabilities of the model, without a complete understanding of the model's limitations.

Noting the shortcomings of the alternative approach to model verification, the results of the comparisons of the predictions made using the proposed first order models and the empirical expressions and guidelines should be viewed as preliminary. While favorable comparisons will lend credence to using the energy-based *Capacity* curve derived from earthquake case histories in remedial ground densification design, such comparisons will not conclusively validate the concept of "energy-based remediation of liquefiable soils." Finally, in line with the philosophy of evaluating simple models by comparisons with higher order models, as well as favorable comparisons with field case histories, a limited discussion is given at the end of the chapter on higher order numerical models.

8.3 Numerical Modeling of Vibro-Compaction

8.3.1 Proposed Model

As discussed in Chapter 7, the vibroflot-soil interaction is very complex. The horizontal/torsional vibrations and the introduction of both water and backfill during vibrations do not lend themselves to being simply modeled. However, with a few simplifying assumptions, the vibratory probe method may be reduced, as a first order approximation, to a rather simple system. For this reason, a first order model is only proposed for the vibratory probe method and not for vibrocompaction.

The mechanisms leading to the breakdown of the soil structure during vibratory probing were briefly discussed in Chapter 7 (Section 7.2.2) and illustrated in Figure 7-13. Although Rayleigh and P-waves contribute, it is assumed that the soil structure is primarily broken down by radially propagating, vertically polarized, shear waves (SV-waves). This assumption is similar to that inherent in the first order model proposed by Holeyman (1997). Based on this assumption, the simple model illustrated in Figure 8-1 is used to compute the amount of energy that is dissipated in the soil surrounding the probe. In this figure, it is shown that the amplitude of the SV-waves decreases as a function of distance from the probe. The decay in the of amplitude of the SV-waves with distance can be attributed to geometrical spreading (i.e., conservation of energy) and to material (or hysteretic) damping in the soil, where the latter is related to the breakdown of the soil structure (i.e., see Chapter 3).

The shear strains resulting from the radially propagating shear waves is given by the following expression (e.g., Newmark 1968, Dowding 1996).

$$\gamma = \frac{v}{v_s} \tag{8-1}$$

where: γ = Shear strain from SV-wave.

v = Particle velocity of SV-wave.

v_s = Shear wave velocity of soil.

In this expression, v and v_s have the same units, resulting in γ being dimensionless.

The peak particle velocity (v) as a function of distance from the probe (r) can be determined from empirical attenuation relations, which will be discussed subsequently in Section 8.3.2. However, first attention is given to v_s. Because v_s is a function of the induced shear strain (γ), Equation (8-1) has to be solved iteratively. A similar procedure to that used in the strain-based liquefaction procedure (Chapter 2, Section 2.2.2) may be employed. The shear wave velocity (v_s) is related to shear modulus (G) by the following expression.

$$G = \frac{v_s^2 \cdot \gamma_t}{g} \qquad \text{(e.g., Richart et al. 1970)} \tag{8-2}$$

where: G = Shear modulus.

v_s = Shear wave velocity.

γ_t = Total unit weight of the soil.

g = Acceleration due to gravity.

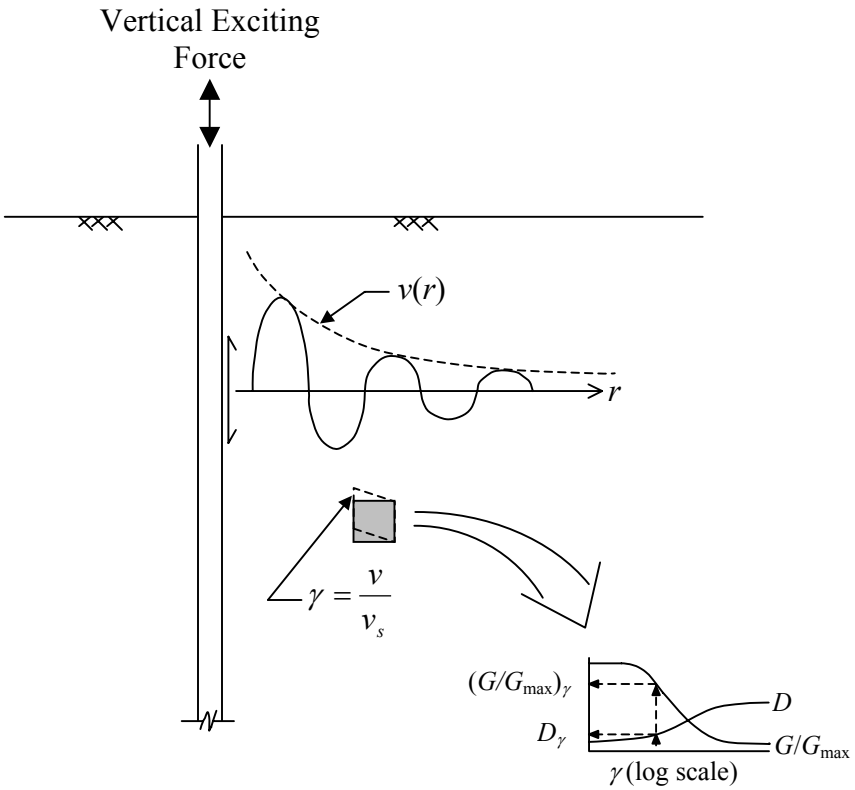

Figure 8-1. First order model of the vibratory probe method.

From substituting Equation (8-2) into Equation (8-1), the resulting expression provides a direct relationship between shear strain (γ) and the shear modulus ratio (G/G_{max}).

$$\gamma = \frac{v}{v_{s\,max} \cdot \sqrt{\frac{G}{G_{max}}}} \tag{8-3}$$

where: γ = Shear strain.

v = Particle velocity of shear wave.

$v_{s\,max}$ = Small strain shear wave velocity of the soil (i.e., $\gamma \leq 10^{-6}$) .

G/G_{max} = Shear modulus ratio.

The iterative solution of Equation (8-3) is shown graphically in Figure 8-2, where in the first iteration a value of G/G_{max} is assumed and γcomputed. In the second iteration, the ratio of G/G_{max} corresponding to γ computed in the first iteration is used. The process is

repeated until the assumed and computed ratios are with in a tolerable error. The Ishibashi and Zhang (1993) shear modulus degradation curves, given previously as Equation (2-16), were used to solve Equation (8-3).

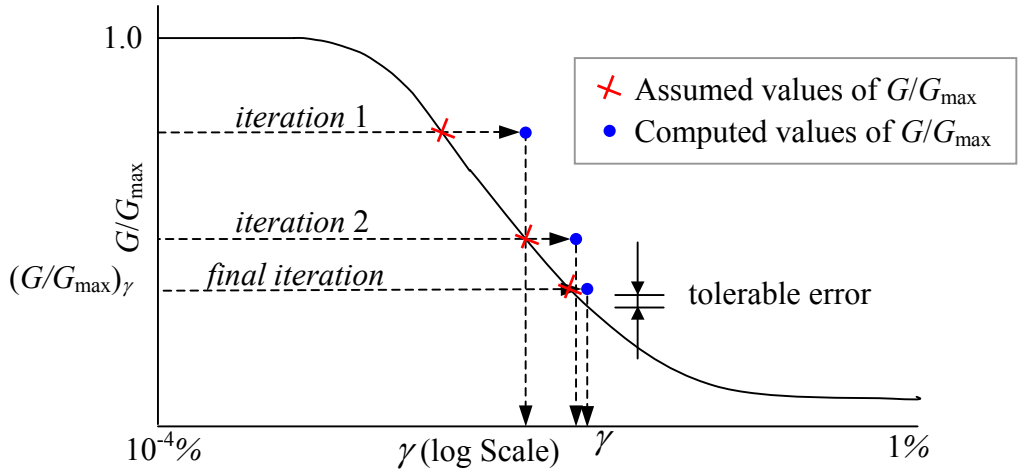

Figure 8-2. Iterative solution of Equation (8-3) to determine the shear-strain (γ) at a given distance from the vibratory probe.

Once γ is determined, the damping and shear modulus ratios are readily determined from the respective degradation curves, as illustrated in Figure 8-3. An expression for the Ishibashi and Zhang (1993) damping degradation curves was given previously as Equation (3-4).

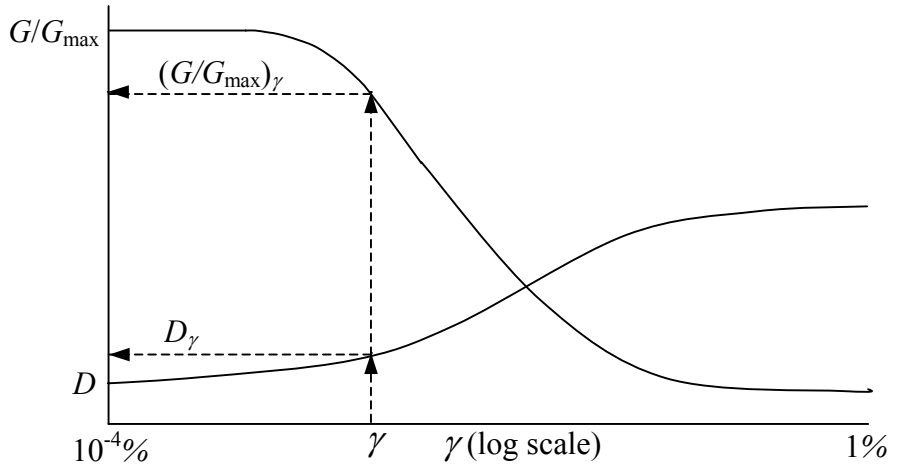

Figure 8-3. The determination of shear modulus and damping ratios from the respective degradation curves.

Knowing G/G_{max}, D, and γ, two important sets of information can be determined. First, using the threshold strain concept presented in Chapter 2 (Section 2.2.2), the maximum possible extent of liquefaction around the probe can be defined by the locus of points where the induced strain equals the threshold strain ($\gamma = \gamma_{th}$; $\gamma_{th} \approx 0.01$ to 0.015%). Second, the cumulative energy dissipated per unit volume of soil, normalized by the initial mean effective confining stress, (i.e., normalized energy demand, *NED*: Section 5.2.3) imparted to the soil by the vibratory probe can be determined. The following series of algebraic manipulations and substitutions results in an expression, Equation (8-4), used to compute *NED*. For reference purposes, the section and equation numbers of expressions and terms presented earlier in this thesis are given.

$$\Delta W_1 = 2\pi \cdot D_\gamma \cdot \tau \cdot \gamma \tag{5-2}$$

$$\tau = G \cdot \gamma = G_{max} \cdot \left(\frac{G}{G_{max}} \right)_\gamma \cdot \gamma$$

$$\Delta W_1 = 2\pi \cdot D_\gamma \cdot G_{max} \cdot \left(\frac{G}{G_{max}} \right)_\gamma \cdot \gamma^2$$

$$NED = \frac{\Delta W_1}{\sigma'_{mo}} \cdot N \tag{5-10}$$

$$N = f \cdot dur$$

$$NED = 2\pi \cdot D_\gamma \cdot G_{\max} \cdot \left(\frac{G}{G_{\max}} \right)_\gamma \cdot \gamma^2 \cdot f \cdot dur \cdot \frac{1}{\sigma'_{mo}}$$

$$NED = D_\gamma \cdot G_{\max} \cdot \left(\frac{G}{G_{\max}} \right)_\gamma \cdot \gamma^2 \cdot \omega \cdot dur \cdot \frac{1}{\sigma'_{mo}} \tag{8-4}$$

where:
- NED = Normalized energy demand (Section 5.2.3).
- ΔW_1 = Dissipated energy per unit volume is one cycle of loading (Section 3.3.2).
- D_γ = Damping ratio (Section 3.3.2).
- G_{max} = Small strain shear modulus (Section 2.2.2)
- $G/G_{\max}$ = Shear modulus ratio.
- γ = Shear strain.
- N = Number of cycles of loading.
- f = Frequency of exciting force (*hz*).
- ω = Frequency of exciting force (*rad/sec*).
- dur = Duration of exciting force (*sec*).
- σ'_{mo} = Initial mean effective confining stress (Section 2.2.2).

Using the above expression for *NED* in conjunction with the expression for the normalized energy capacity of the soil (*NEC*: Equation (5-11), Figure 5-11), the extent of induced liquefaction can be predicted as a function of the duration of vibrations. *NEC* is defined as the cumulative energy dissipated per unit volume of soil, normalized by the initial mean effective confining stress, required to induce liquefaction.

8.3.2 Attenuation Relationships

In order to solve Equation (8-4), attention is returned to attenuation relations for determining peak particle velocity (v) as a function of distance from the probe (r). Using empirical attenuation relationships is the most direct method for determining v.

Attenuation relations are of two general types depending of the required information needed to predict the amplitude of vibrations (Woods and Jedele 1985). The first type requires the source energy to be known. The second type requires the amplitude of vibrations to be known at one point to predict the amplitudes of vibrations at other points. Inherent to both types of relations are empirical constants, which are dependent on parameters such as the soil/site conditions.

Clearly, using attenuation relations that predict peak particle velocities (v) as functions of the source energy would fit best with the theme of this thesis. Unfortunately, the empirical constants associated with this class of attenuation relations have primarily been established for impact type energy sources such as used in impact pile driving, deep dynamic compaction, and explosive compaction and have not been developed for vibratory type sources. The most likely reason for this is that the source energy for vibratory probes is not constant but rather increases as the soil densifies. This phenomenon was briefly discussed in Chapter 7 in relation to current draw of electric vibrators. As a result, it is difficult to readily quantify the source energy by a single value, and therefore, it is difficult to establish the empirical constants for the energy-source type of attenuation relations.

On the contrary, attenuation relations requiring the amplitude of vibrations to be known at one point in order to predict the amplitudes of vibrations at other points have been used for both impact type and vibratory sources. Considering only geometrical spreading, these attenuation relations take the form:

$$w_2 = w_1 \cdot \left(\frac{r_1}{r_2} \right)^n \qquad \text{(e.g., Woods and Jedele 1985)} \qquad (8\text{-}5)$$

where: w_1 = Known amplitude of vibration at distance r_1 from the source.

w_2 = Unknown amplitude of vibration at distance r_2 from the source.

n = Geometric damping coefficient; see Table 8-1.

Table 8-1. Geometric damping coefficients. (Adapted from Gutowski and Dym 1976 and Kim and Lee 1998).

Source Location	Source Type	Example Sources	Induced Wave	n	Monitoring Location
Surface	Point	Friction pile driving, train loading (<16 passenger cars)	Body Wave	2.0	Surface
				1.0	At-Depth
		Dynamic compaction	Surface Wave	0.5	Surface
	Infinite Line	Train loading (>16 passenger cars)	Body Wave	1.0	Surface
				0.5	At-Depth
		—	Surface Wave	0	Surface
At-Depth	Point	At-depth Blasting	Body Wave	1.0	At-Depth
	Infinite Line	—		0.5	At-Depth

To account for material damping, an additional term is added to Equation (8-5):

$$w_2 = w_1 \cdot \left(\frac{r_1}{r_2}\right)^n \cdot \exp\left[-\alpha \cdot (r_2 - r_1)\right] \qquad (8\text{-}6)$$

where: α = Empirical coefficient of attenuation that varies as a function of soil/site conditions (1/distance); see Table 8-2.

Table 8-2. Proposed Classification of Earth Materials by Attenuation Coefficient. (Adapted from Woods and Jedele 1985).

Class	Attenuation Coefficient α	Description of Material
I	5*hz*: 0.01 to 0.03 (1/*m*) 0.003 to 0.01 (1/*ft*) 50*hz*: 0.10 to 0.30 (1/*m*) 0.03 to 0.10 (1/*ft*)	Weak or Soft Soils – lossy soils, dry or partially saturated peat and muck, mud, loose beach sand, and dune sand, recently plowed ground, soft spongy forest or jungle floor, organic soils, top soils. (shovel penetrates easily)
II	5*hz*: 0.003 to 0.01 (1/*m*) 0.001 to 0.003 (1/*ft*) 50*hz*: 0.03 to 0.10 (1/*m*) 0.01 to 0.03 (1/*ft*)	Competent Soils – most sands, sandy clays, silty clays, gravel, silts, weathered rock. (can dig with shovel)
III	5*hz*: 0.0003 to 0.003 (1/*m*) 0.0001 to 0.001 (1/*ft*) 50*hz*: 0.003 to 0.03 (1/*m*) 0.001 to 0.01 (1/*ft*)	Hard Soils – dense compacted sand, dry consolidated clay, consolidated glacial till, some exposed rock. (cannot dig with shovel, must use pick to break up)
IV	5*hz*: < 0.0003 (1/*m*) < 0.0001 (1/*ft*) 50*hz*: < 0.003 (1/*m*) < 0.001 (1/*ft*)	Hard, Competent Rock – bedrock, freshly exposed hard rock. (difficult to break with hammer)

The α values presented in Table 8-2 were established from field data collected over a twenty year period (Woods and Jedele 1985). As discussed in Richart et al. (1970), α is frequency dependant. The following expression relates α and the frequency of the vibrations.

$$\alpha = \pi \cdot \frac{f}{Q \cdot v_s} = \pi \cdot \frac{2 D f}{v_s} \tag{8-7}$$

where: α = Empirical coefficient of attenuation that varies as a function of

soil/site conditions (1/distance); see Table 8-2.

f = Frequency of vibrations (*hz*).

v_s = Shear wave velocity of the soil.

Q = Quality factor.

$$= \frac{1}{2 \cdot D}$$

D = Damping ratio of the soil (Chapter 3, Section 3.3.2).

From Equation (8-7), the α values for two different frequencies may be related by the following expression:

$$\alpha_2 = \alpha_1 \cdot \left(\frac{f_2}{f_1} \right) \tag{8-8}$$

where: α_1 = Known α value corresponding to frequency f_1 (1/distance).

α_2 = Unknown α value corresponding to frequency f_2 (1/distance).

Table 8-2 gives the α values for two different frequencies: 5 and 50*hz*. Using Equation (8-8), α values for other frequencies can be determined.

As a final observation, Equation (8-7) shows that α increases proportionally to the damping ratio of the soil (D). Accordingly, it is expected that loose soil deposits will have larger α values than denser deposits; this trend is confirmed by the empirical data presented in Table 8-2.

The expressions representing attenuation due to geometrical spreading only and geometrical spreading plus material damping (i.e., Equations (8-5) and (8-6), respectively) are plotted in Figure 8-4. Also shown in this figure are peak particle velocities measured during deep dynamic compaction: $W = 6 tons$, $H = 27 m$. As may be observed from this figure, the influence of material damping can be significant.

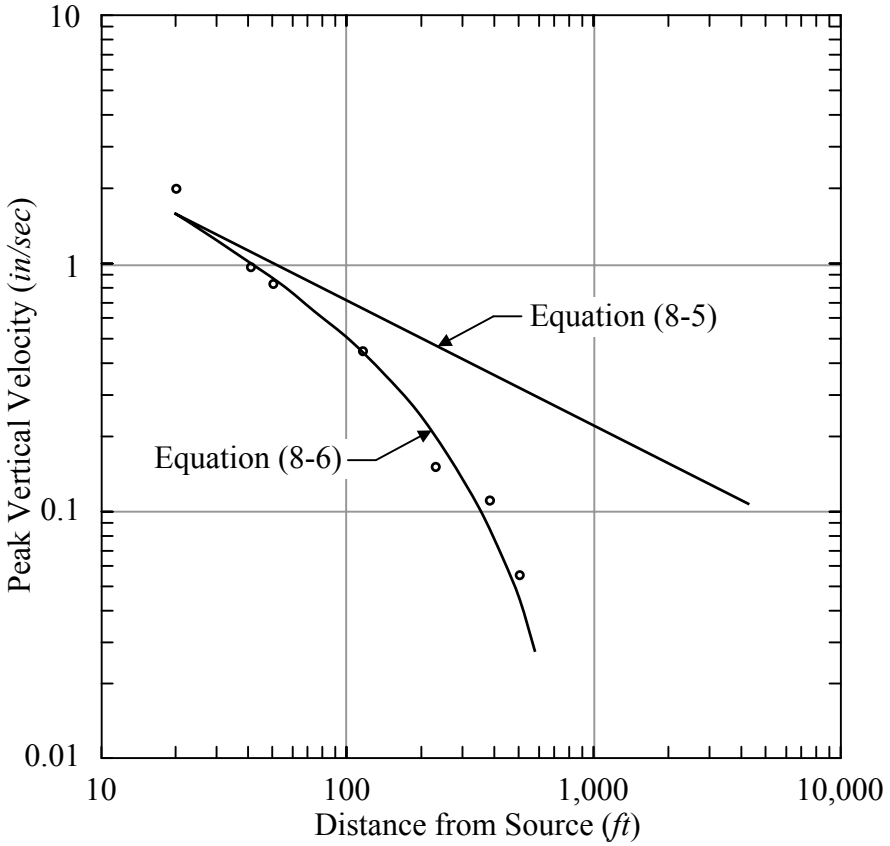

Figure 8-4. Comparison of attenuation relations given by Equation (8-5) (i.e., geometrical spreading only) and given by Equation (8-6) (i.e., combined geometrical spreading and material damping). The data points shown in the plot are peak particle velocities resulting from the dropping of a 6*ton* tamper from 27*m*. (Adapted from Woods and Jedele 1985).

A limited literature review was performed concerning attenuation relations specific to vibro-compaction. In regards to the vibratory probe method, Van Impe et al. (1994) state: "The attenuation coefficient α for vibratory compaction varies in saturated clean sands typically between 0.05 and $0.10m^{-1}$. In partially saturated to dry sands α can rise to $0.5m^{-1}$." However, no mention is given to the frequencies corresponding to the stated α values. Figure 8-5 shows measured peak accelerations as a function of distance from Y- and double-Y probes for two different excitation frequencies. Although the data points shown in this figure are not distinguished as a function of the excitation frequency, it appears to have little influence on the peak accelerations. However, as may be observed

from the following expression, the corresponding peak particle velocities (v) for the two excitation frequencies will be very different.

$$v = \frac{a \cdot g}{2\pi f} \tag{8-9}$$

where: v = Peak particle velocity (consistent units with g).

a = Peak acceleration (g).

g = Acceleration due to gravity (same units as v).

f = Excitation frequency (hz).

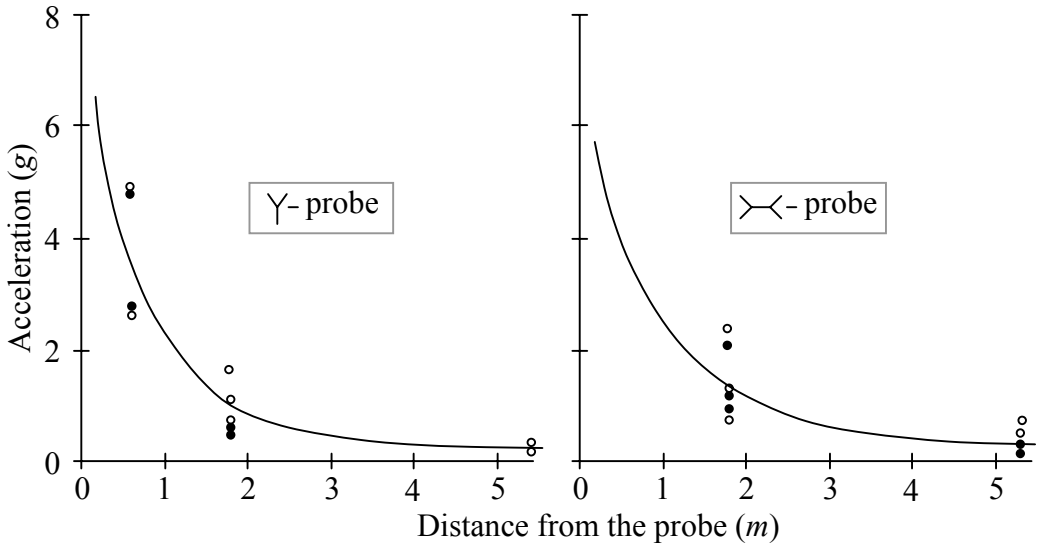

Figure 8-5. Attenuation of peak ground acceleration with distance from the vertically vibrating probe excited at 16 and 25hz. (Adapted from Van Impe et al. 1994).

The α values corresponding to the curves shown in Figure 8-5 were not given by Van Impe et al. (1994), but from simple trial and error, the author found that $\alpha = 0.45$ and $0.4m^{-1}$ provide reasonable approximations for the Y- and double-Y curves, respectively. Using the form of Equation (8-6), the curves shown in Figure 8-5 may be approximated by the following expressions.

Y-Probe:

$$a_{\max} = 3.1 \cdot \left(\frac{0.74}{r}\right)^{0.5} \cdot \exp\left[-0.45 \cdot (r - 0.74)\right] \tag{8-10a}$$

Double-Y Probe:

$$a_{\max} = 2.5 \cdot \left(\frac{0.97}{r} \right)^{0.5} \cdot \exp\left[-0.40 \cdot (r - 0.97) \right] \qquad (8\text{-}10b)$$

where: $a_{\max}$ = Peak acceleration (g).

r = Distance from the probe (m).

Based on the statements of Van Impe et al. (1994) presented above regarding the range of α for different soil conditions, it is likely that the data shown in the above plots were measured in partially saturated or dry sand.

Holeyman (1997) proposed the following attenuation relation for peak accelerations as a function of distance from a Y-probe.

$$\text{“ } A_r \div (d.(1 + b.d))^{-1/2}.e^{-a.d} \qquad (8\text{-}11a)$$

where: A_r = Amplitude of vibration at radial distance r

d = $(r^2 + h^2)^{1/2}$, with h = probe ribs equivalent focal depth

b = geometric damping accentuation factor

a = intrinsic soil damping”

Holeyman (1997) goes on to give the following values for the variables in this expression: $h = 0.7m$, $b = 1/30m^{-1}$, and $a = 0.\ 03m^{-1}$. Additionally, a plot of the above expression is shown in comparison to measured acceleration values for several excitation frequencies, which is reproduced as Figure 8-6. The author is uncertain how to interpret Equation (8-11a). If it is interpreted as:

$$A_r = \frac{1}{\sqrt{d \cdot (1 + bd)}} \cdot e^{-ad} \qquad (8\text{-}11b)$$

where A_r is assumed to be in g and the horizontal axis in Figure 8-6 is assumed to be r, then the resulting plot does not match that given in Holeyman (1997), as shown in Figure 8-6. Several other interpretations of Equation (8-11a) were made but none resulted in a match of the curve presented in Holeyman (1997). Keeping the same form of Equation (8-11b), the following expression was found to give a good approximation of the curve presented in Holeyman (1997); see Figure 8-6.

$$A_r = \frac{1}{\sqrt{d \cdot (1 + bd) \cdot 9.81}} \cdot e^{-ad} \qquad \text{(8-11c)}$$

where: A_r = Amplitude of vibration at radial distance r (g).

d = $(r^2 + h^2)^{1/2}$

r = Radial distance from probe (m).

h = 0.7

b = 1 /4.75 (as opposed to 1/30 as proposed in Holeyman 1997)

a = 0.03

Alternatively, the data shown in Figure 8-6 may be fit by the following expression, as shown in Figure 8-6.

$$a_{\max} = 0.14 \cdot \left(\frac{2.66}{r}\right)^{0.5} \cdot \exp\left[-0.05 \cdot (r - 2.66)\right] \qquad \text{(8-11d)}$$

where: $a_{\max}$ = Peak acceleration (g).

r = Radial distance from the probe (m).

The only clear trend that can be observed from the data shown in Figure 8-6 is that at greater radial distances the peak accelerations tend to be less for the 10.5hz data than for the two other excitation frequencies. Similar to the data shown in Figure 8-5, no clear trend can be observed in acceleration values for 15.6 and 21.0hz. However, the corresponding velocities will differ. For comparison purposes, the α values presented in Table 8-2 range from 0.01 to 0.03m^{-1} for Class I soils subjected to a 5hz excitation. Using Equation (8-8), the range becomes 0.04 to 0.12m^{-1} for a 20hz excitation, which is consistent with $\alpha = 0.05m^{-1}$ in Equation (8-11d).

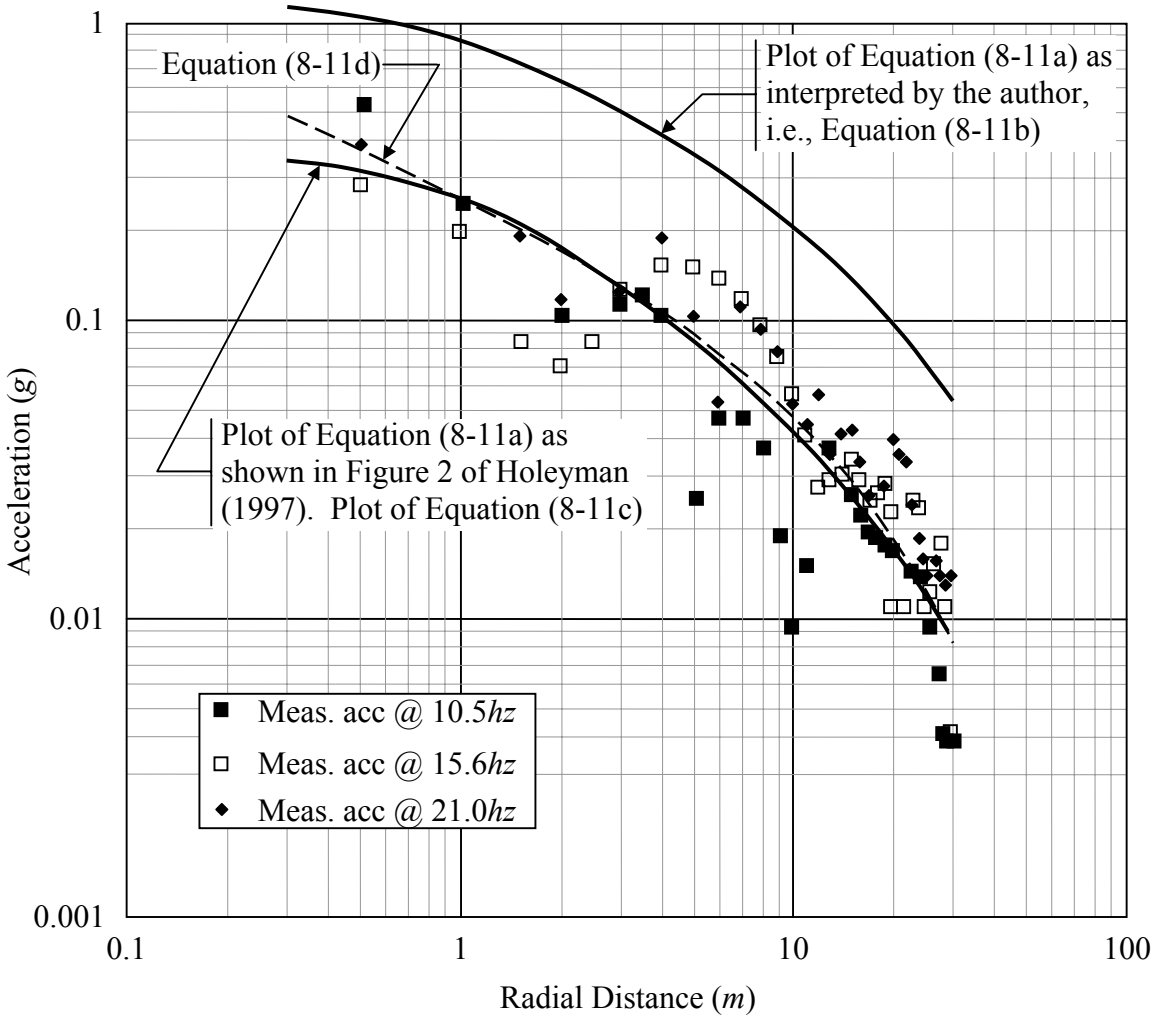

Figure 8-6. Comparison of attenuation expressions to measured field data for three excitation frequencies. (Adapted from Holeyman 1997).

The final set of attenuation data reviewed is that presented in Baez (1995), which is shown in Figure 8-7. These data were recorded during the placement of stone columns using a Keller bottom-feed "S" vibrator with a maximum 20*ton* centrifugal force and a 165*hp* motor (stone column: vibrocompaction with gravel backfill).

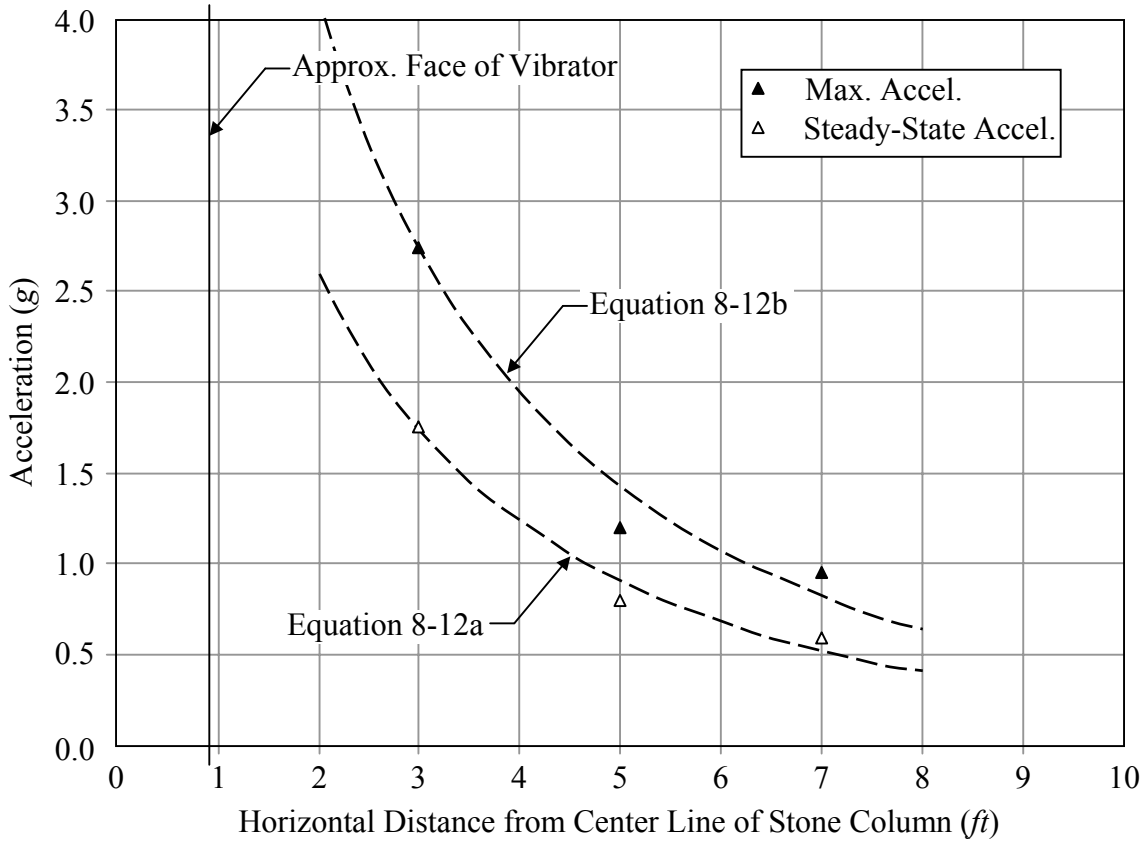

Figure 8-7. Measured vibration levels at a depth of 14*ft* during the placement of stone columns. (Adapted from Baez 1995).

The data presented in Baez (1995) is unique in that Baez distinguishes between peak and steady state vibration amplitudes, where the steady state amplitude is defined as that lasting 5 consecutive seconds or longer. Assuming the form of the attenuation relation of Equation (8-6), the following expressions provide a reasonable fit of the steady state and peak accelerations, respectively.

$$a_{steady\ state} = 1.7 \cdot \left(\frac{3}{r}\right)^{0.5} \cdot \exp\left[-0.2 \cdot (r-3)\right] \tag{8-12a}$$

$$a_{\max} = 2.7 \cdot \left(\frac{3}{r}\right)^{0.5} \cdot \exp\left[-0.2 \cdot (r-3)\right] \tag{8-12b}$$

where: $a_{steady\ state}$ = Steady state acceleration (g).

a_{max} = Peak acceleration (g).

r = Radial distance from the probe (ft).

As may be observed from Equations (8-12a) and (8-12b) and the data plotted in Figure 8-7, the ratio of $a_{steady\ state}$ to a_{max} is essentially independent of distance from the probe and is approximately 0.633.

Finally, assuming oscillatory motions, the accelerations computed by any of the above expressions are related to the corresponding particle velocity by:

$$v = \frac{a \cdot g}{\omega} \tag{8-13}$$

where: v = Particle velocity.

a = Acceleration (g).

g = Acceleration due to gravity.

ω = Excitation frequency (rad/sec).

In this expression, v and g have consistent units.

8.3.3 Comparison of Proposed First Order Model Predictions with Empirical Guidelines

General trends in the predictions of the first order model proposed above are compared with the empirical guidelines presented in Chapter 7 (i.e., the typical spacing of compaction points for the vibratory probe method ranges from 1 to 2m (Broms 1991)). For a triangular grid pattern, the distance from a compaction point to the center of the compaction points is approximately $0.6 \cdot S$, as shown in Figure 8-8, where S is the spacing between the compaction points. Based on this, the lateral extent of improvement for a single compaction point is approximated as $0.6 \cdot S$, resulting in a range of about 2 to 4ft.

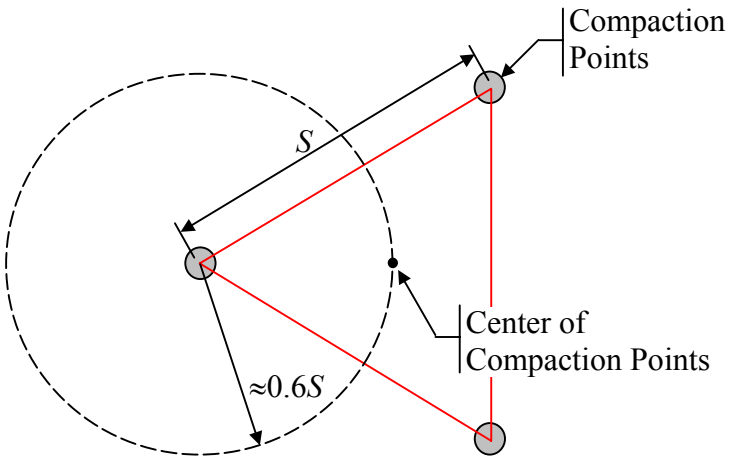

Figure 8-8. For a triangular grid pattern, the distance from a compaction point to the center of the compaction points is approximately 60% of the distance between the compaction points.

Using the proposed first order model, the lateral extent of liquefaction was estimated for a clean sand profile having a constant $N_{1,60} = 5 blws/ft$ with depth, $\gamma_t = 125 pcf$, and a depth to the groundwater table of $10 ft$. The vibratory probe was assumed to be excited at $20 hz$, and Equations (8-11d) and (8-13) were used to compute the peak particle velocity as a function of distance from the probe. Assuming a threshold strain of 0.01%, the maximum extent of liquefaction was determined by the iterative solution of Equation (8-3), the results of which are shown in Figure 8-9a. The boundary shown in this figure defines the distance from the probe to the locus of points in the profile where the induced shear strain equals 0.01%. The *Demand* and *Capacity* expressions (Equations (8-4) and (5-11), respectively) can be used to estimate the duration of the vibrations required to induce liquefaction. Such calculations were performed, and the results are shown in Figure 8-9b. In this figure, the extent of liquefaction (or liquefaction front) is shown for 0.5, 1, 5, 10, and $15 sec$ of vibrations, where at $15 sec$ the liquefaction front reaches its final location. In addition to the model predictions, the empirical range of the lateral extent of improvement is superimposed on Figures 8-9a and 8-9b.

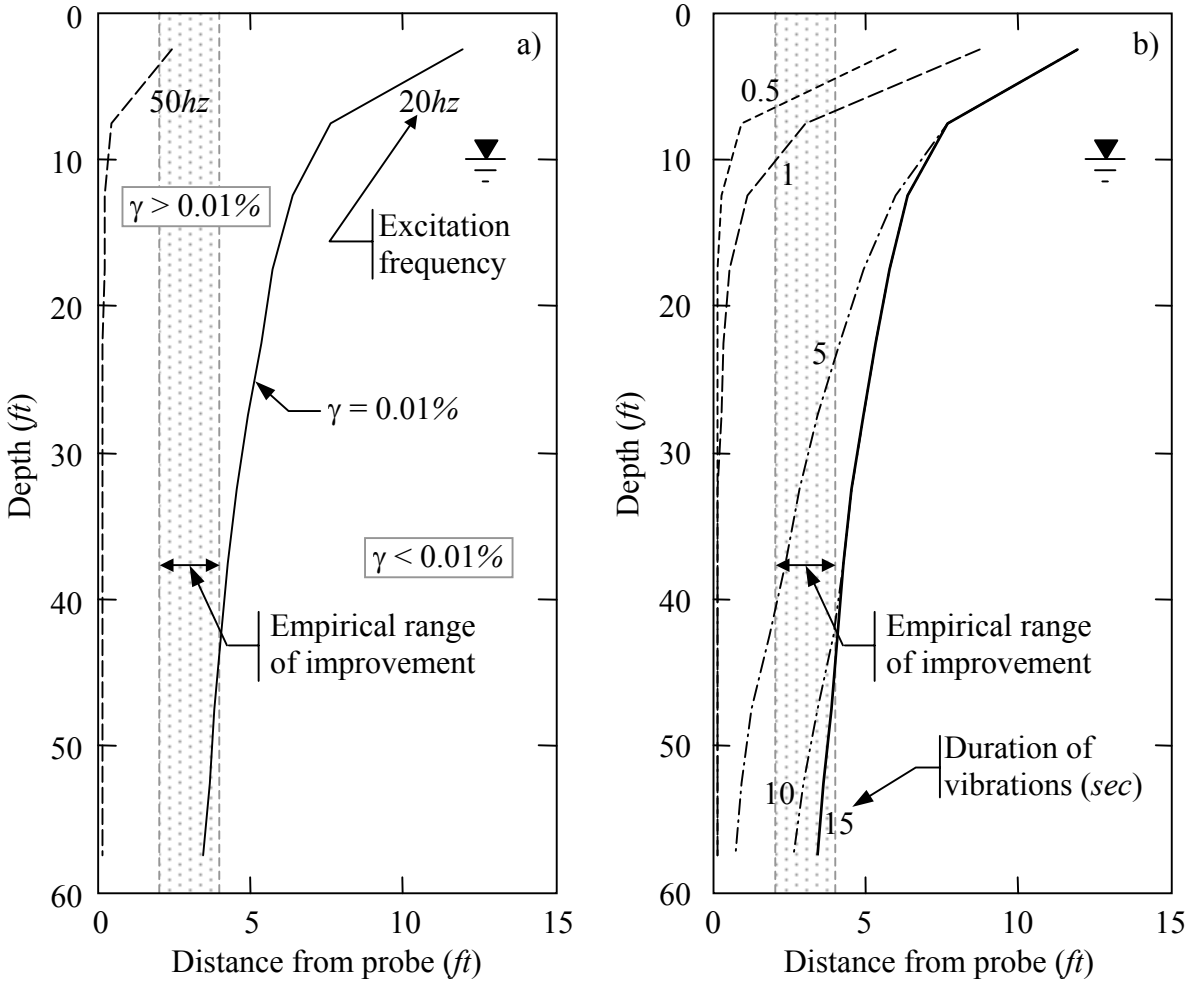

Figure 8-9. Simple model predictions using peak particle velocities: a) The maximum extent of liquefaction for 20 and 50*hz* excitation frequencies, b) Liquefaction fronts for 0.5, 1, 5, 10, and 15*sec* of vibrations at 20*hz*.

Two immediate observations can be made concerning the plots shown in Figure 8-9. First, the model's prediction for the maximum extent of liquefaction is larger than the empirical range of improvement. Second, the maximum extent of liquefaction is predicted to be reached in 15*sec*, which is rather quick. The most likely reason for both of these observations is that the empirical attenuation relation used is for peak particle velocity and not steady state particle velocity. To account for this, the ratio of peak to steady state accelerations determined from the data presented in Figure 8-7 (i.e., 0.633) was used to adjust the peak particle velocities computed using Equation (8-11d). Using

the adjusted velocities, analogous results to those shown in Figure 8-9 are shown in Figure 8-10.

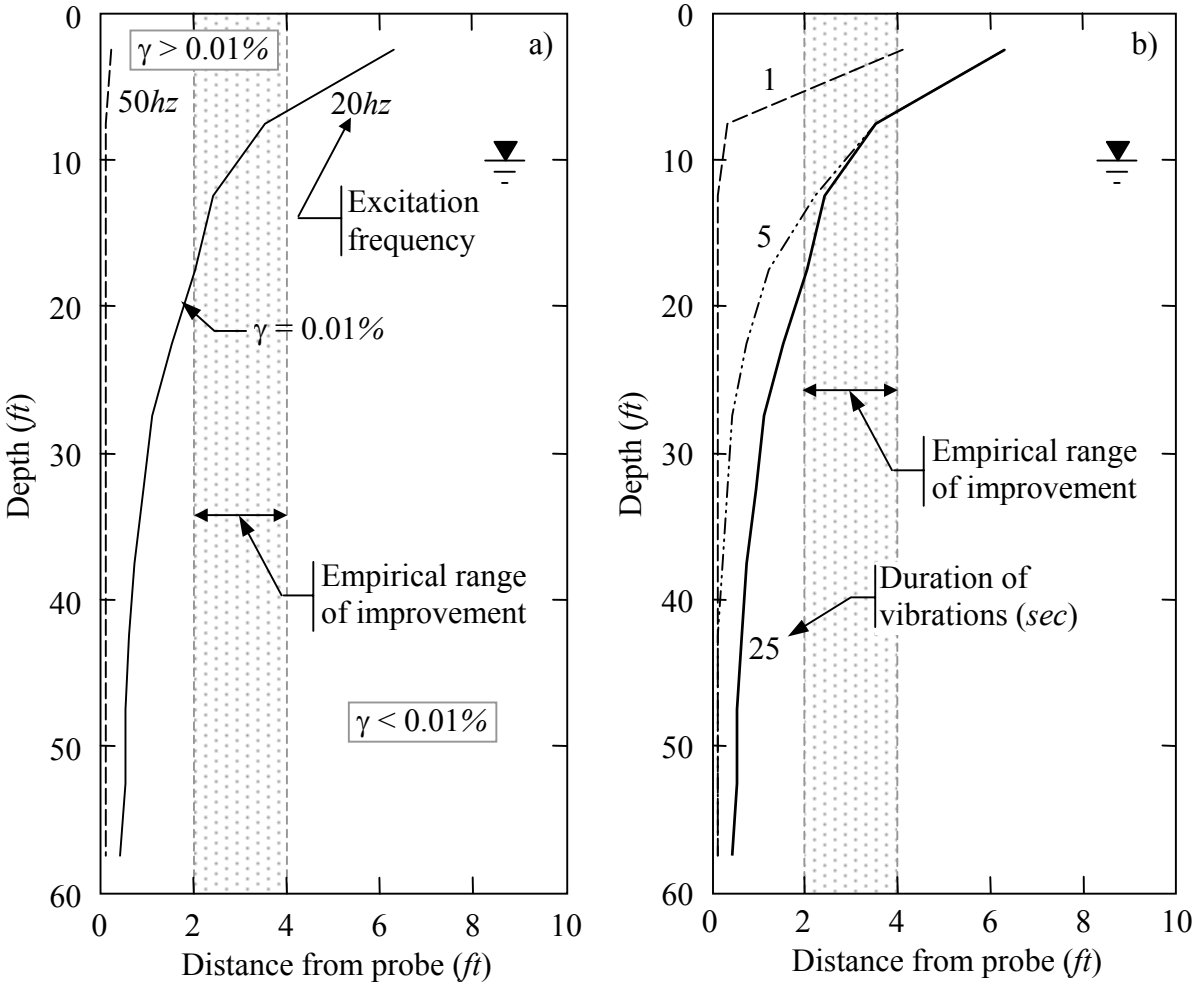

Figure 8-10. Simple model predictions using steady state particle velocities: a) The maximum extent of liquefaction for 20 and 50*hz* excitation frequencies, b) Liquefaction fronts for 1, 5, and 25*sec* of vibrations at 20*hz*.

As may be observed from Figure 8-10, using the steady state particle velocities results in a reduction in predicted extent of liquefaction and an increase in the required vibration time for the liquefaction front to reach its final position. However, the predicted extent of liquefaction now under-predicts the extent of improvement in comparison with the empirical range. Although it may seem that the steady state particle velocities assumed are too low, this might not be the cause of the under-prediction. As may be recalled from

Chapter 7, improvement from vibro-compaction results from both the densification of the soil and from increased lateral confining pressure. The proposed simplified model does not account for the latter mechanism. Accordingly, the extent of improvement is expected to extend beyond the boundary of predicted liquefaction. Additionally, although the time required for the liquefaction front to reach its final position (i.e., 25*sec*) may still seem short, this may not be the case. In typical densification programs, the process of repeated insertion and withdrawal is employed, which extends the vibration time per compaction point over that required to induce liquefaction in a virgin profile.

Several other observations can be made concerning the model predictions in Figure 8-10. As shown in Figure 8-10b, soils at depth are predicted to require greater vibration times for the liquefaction front to reach its final position. This is consistent with field observations. Furthermore, the conical shape of the predicted liquefaction zone is also consistent with field observations. For liquefied soil, settlements typically range from about 2 to 10% of the depth of the liquefied deposit (Tokimatsu and Seed 1987). Based on this, the magnitude of settlement would decrease with increasing distance from the probe, resulting in a conical surface depression. As may be seen in Figure 8-11, such conical depressions occur in the field.

Finally, in Figures 8-9a and 8-10a, the boundaries for the extent of liquefaction are predicted for 50*hz* excitation frequency, in addition to the 20*hz* boundaries discussed above. The boundaries corresponding to 50*hz* are considerably less than those for 20*hz*. The significance of this is the following. To avoid getting the probe stuck in the profile, densification is undesirable during initial insertion of the probe to the desired depth of improvement; compaction occurs as the probe is withdrawn. From the results shown in Figures 8-9a and 8-10a, it can be seen that initial penetration at high a frequency and withdrawal at a lower frequency will achieve this goal.

Figure 8-11. Conical surface depression created by vibrocompacting without backfill. (Photo courtesy of W.S. Degen, Vibro Systems, Inc.).

8.4 Numerical Modeling of Deep Dynamic Compaction

The first order model proposed for deep dynamic compaction (DDC) consists of two parts: the approximation of the input motion and the response of the soil at depth in the profile. Each will be presented in turn, starting with the approximation of the input motion.

8.4.1 Approximate Input Motion for Deep Dynamic Compaction

The approach used to compute the motion resulting from a tamper impacting the surface of a soil profile is similar to that used in machine foundation design (i.e., dynamic soil structure interaction). In this approach, the soil profile is represented by a viscously damped, single degree of freedom oscillator, such as shown in Figure 8-12. The spring stiffness and the damping coefficient are determined by the expressions proposed by Lysmer and Richart (1966), Equations (8-14a) and (8-14b), respectively.

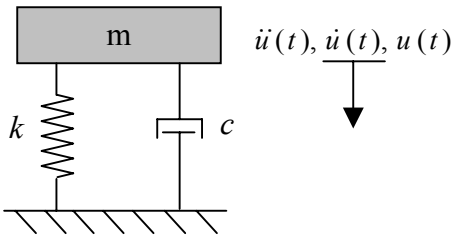

Figure 8-12. Viscously damped, single degree of freedom oscillator used to represent the soil profile.

$$k = \frac{4Gr}{1-\nu} \tag{8-14a}$$

$$c = \frac{3.4}{1-\nu} \cdot r^2 \cdot \sqrt{\frac{G\gamma_t}{g}} \tag{8-14b}$$

where:

k	=	Spring stiffness.
G	=	Shear modulus of the soil.
r	=	Equivalent radius of the tamper.
ν	=	Poisson's ratio.
c	=	Viscous damping coefficient.
g	=	Acceleration due to gravity.
γ_t	=	Total unit weight of the soil.

Assuming that upon impact the mass moves in unison with the soil profile and ignoring the influence of gravity acting on the tamper after impact, the governing differential equation for the motion of the mass is given by the following expression.

$$m\ddot{u}(t) + c\dot{u}(t) + ku(t) = 0 \qquad \text{(e.g., Chopra 1995)} \tag{8-15}$$

where:

$\ddot{u}(t)$	=	Acceleration of mass.
$\dot{u}(t)$	=	Velocity of mass.
$u(t)$	=	Displacement of mass.
m	=	Mass of tamper plus participating soil mass.

By dividing through by m, Equation (8-15) for the motion of the mass can be written in alternate form:

$$\ddot{u}(t) + 2\beta\omega_n \dot{u}(t) + \omega_n^2 u(t) = 0 \tag{8-16}$$

where: ω_n = Natural frequency of oscillator (*rad/sec*).

$$= \sqrt{\frac{k}{m}}$$

β = Damping ratio (see Equation (3-5)).

$$= \frac{c}{2\sqrt{km}}$$

For a less than critically damped system, the general solution for Equation (8-16) is given by the following expression (e.g., Chopra 1995).

$$u(t) = e^{-\beta\omega_n t} \cdot \left[u_o \cos(\omega_D t) + \frac{\dot{u}_o + \beta\omega_n u_o}{\omega_D} \sin(\omega_D t) \right] \tag{8-17}$$

where: ω_D = Damped natural frequency of oscillator (*rad/sec*).

$$= \omega_n \sqrt{1 - \beta^2}$$

u_o = Displacement of oscillator at $t = 0$.

$\dot{u}_o$ = Velocity of oscillator at $t = 0$.

Inherent to the solution given by Equation (8-17), m is assumed only equal to the mass of the tamper and the mass of the participating soil is not included. Given the first order approximation of the proposed model, this assumption is not considered to decrease the accuracy of the computed results beyond the desired limit. Roesset et al. (1994) give a more detailed discussion on the significance of this assumption.

Finally, by designating $t = 0$ as the time of impact, the following initial boundary conditions apply.

Impact velocity: $\dot{u}_o = \sqrt{2gH}$

Initial displacement: $u_o = 0$

Substituting the above initial boundary conditions into Equation (8-17) and differentiating results in the following expressions for displacement, velocity, and acceleration time histories.

$$u(t) = \frac{\dot{u}_o}{\omega_D} \cdot e^{-\beta\omega_n t} \cdot \sin(\omega_D t) \tag{8-18}$$

$$\dot{u}(t) = \frac{\dot{u}_o}{\omega_D} \cdot \left[-\beta\omega_n e^{-\beta\omega_n t} \cdot \sin(\omega_D t) + \omega_D e^{-\beta\omega_n t} \cdot \cos(\omega_D t) \right] \tag{8-19}$$

$$\ddot{u}(t) = \frac{\dot{u}_o}{\omega_D} \cdot e^{-\beta\omega_n t} \cdot \left[\beta^2\omega_n^2 \cdot \sin(\omega_D t) - 2\beta\omega_n\omega_D \cdot \cos(\omega_D t) - \omega_D^2 \cdot \sin(\omega_D t) \right] \tag{8-20}$$

The above expressions are for an *elastic* single degree of freedom oscillator. However, it is known that significant plastic deformations occur around the tamper impact zone (i.e., craters form). To account for the soil non-linearity, degraded values for the shear modulus (G) are used in computing the spring and damping constants (k and c, respectively). The degraded G is determined iteratively using shear modulus degradation curves, which requires a procedure for computing the deviatoric shear strain induced in the soil from the impacting tamper. The following procedure is proposed.

Starting with the small strain soil properties, the maximum acceleration for the soil profile is determined as:

$$a_{\max} = \max\left|\ddot{u}(t)\right| \tag{8-21}$$

From $a_{\max}$ and the dimensions of the tamper, the contact stress between the impacting tamper and soil surface can be determined as:

$$\begin{aligned} \sigma_{\max} &= \frac{F_{\max}}{A} \\ &= \frac{ma_{\max}}{A} \\ &= \frac{Wa_{\max}}{gB^2} \end{aligned} \tag{8-22}$$

where: σ_{max} = Maximum normal stress.

a_{max} = Peak acceleration.

F_{max} = Maximum force imposed by the impacting tamper.

A = Contact area between tamper and soil profile.

W = Weight of tamper.

g = Acceleration due to gravity.

B = Length of square contact area of tamper and soil.

For axi-symmetric conditions, axial stress and axial strain are related by Hooke's law:

$$\varepsilon_a = \frac{\sigma_a}{E_y} - \frac{2\nu}{E_y}\sigma_h \qquad \text{(e.g., Davis and Selvadurai 1996)} \qquad (8\text{-}23a)$$

where: ε_a = Axial strain.

σ_a = Axial stress.

E_y = Young's modulus.

ν = Poisson's ratio.

σ_h = Lateral stress.

However, the use of this expression requires the knowledge of the variation of lateral stress (σ_h) in response to changes in the axial stress (σ_a) induced by the impacting tamper. To avoid the complexities involved in solving Equation (8-23a) and associated equations, cone models are often used in dynamic soil structure interaction analyses (e.g., Wolf 1994). In such models, the elastic half space is replaced by a truncated cone, wherein the lateral stress is assumed equal to zero ($\sigma_h = 0$); see Figure 8-18. This effectively reduces the problem to one dimension, and for the condition of maximum induced stress, Equation (8-23a) becomes:

$$\varepsilon_{a\,max} = \frac{\sigma_{max}}{E'} \qquad (8\text{-}23b)$$

where: $\varepsilon_{a\,max}$ = Maximum induced axial strain.

σ_a = Maximum induced axial stress.

E' = Soil modulus, the value of which is discussed subsequently.

The deviatoric shear strain resulting from the axial loading of the one-dimensional model is given by the following expression.

$$\gamma_{dev} = \varepsilon_a - \varepsilon_h \tag{8-24}$$

where: γ_{dev} = Deviatoric shear strain.

ε_a = Axial strain.

ε_h = Lateral strain.

The axial and lateral strains are related by Poisson's ratio (ν):

$$\nu = \frac{-\varepsilon_h}{\varepsilon_a} \Rightarrow -\varepsilon_h = \nu\varepsilon_a \tag{8-25}$$

Finally, through a series of substitutions, the maximum induced deviatoric shear strain can be expressed as follows:

$$\gamma_{dev\max} = (1+\nu)\frac{Wa_{\max}}{gB^2E'} \tag{8-26}$$

In this expression, Poisson's ratio (ν) is an intrinsic material property and the soil modulus (E') is a both a material property and a function of the boundary/stress conditions. The influence of the boundary conditions on E' can be observed from the two extremes: zero lateral stress and zero lateral strain. For the case of zero lateral stress, shown in Figure 8-13a, E' is equal to Young's modulus (E_y), which is given by Equation (8-27).

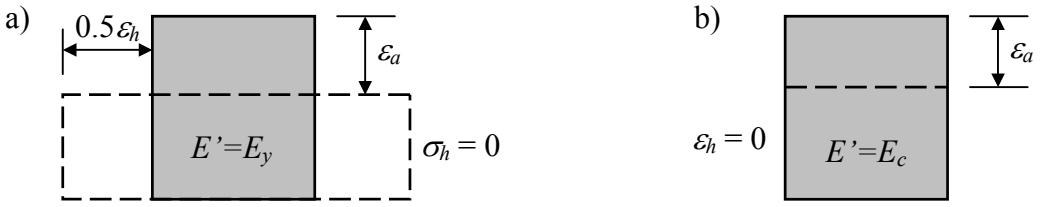

Figure 8-13. The influence on boundary conditions on E'. a) Condition of zero lateral stress, b) Condition of zero lateral strain.

$$E_y = 2G(1+\nu) \tag{8-27}$$

where: E_y = Young's modulus.

G = Shear modulus.

ν = Poisson's ratio.

Similarly, for the condition of zero lateral strain, shown in Figure 8-13b, *E'* is equal to the constrained modulus (E_c), which is given by Equation (8-28).

$$E_c = \frac{2G(1-\nu)}{1-2\nu} \tag{8-28}$$

where: E_c = Constrained modulus.

G = Shear modulus.

ν = Poisson's ratio.

As Poisson's ratio approaches zero, E_c and E_y become equal, as shown in Figure 8-14. However, as Poisson's ratio increases, E_c and E_y differ significantly. The question now becomes: which value of *E'* is appropriate for the boundary conditions governing the response of a mass impacting the surface of a soil profile? No clear consensus is given in the literature on dynamic soil structure interaction, but the value determined as follows is consistent with the previous assumptions made in the development of this model.

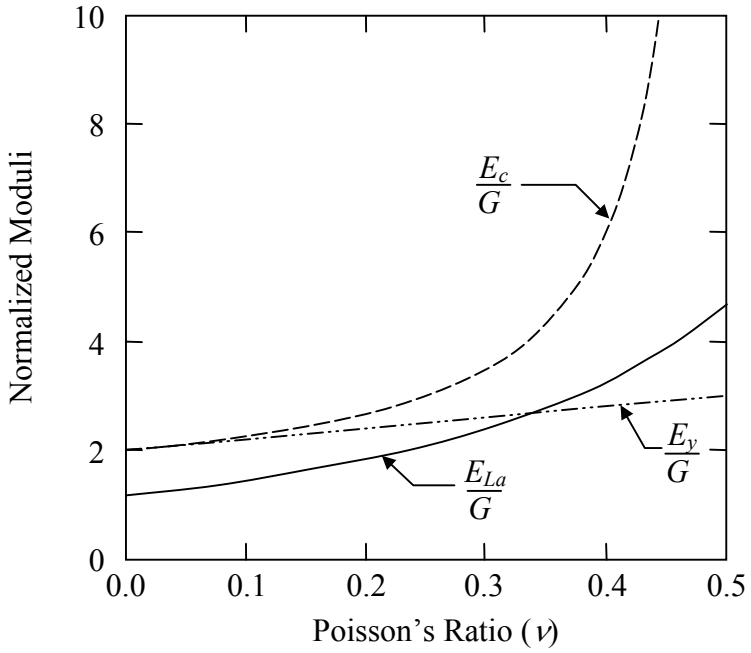

Figure 8-14. Comparison of E_y, E_c, and E_{La} as a function of Poisson's ratio.

From wave propagation theory, it can be shown that an infinitely long rod can be terminated and replaced with a dashpot having a damping coefficient (c) given by Equation (8-29), and no reflection of a propagating wave will occur (e.g., Kramer 1996). This is shown conceptually in Figure 8-15.

$$c = \rho V A \tag{8-29}$$

where: c = Damping coefficient.

ρ = Mass density of rod.

V = Propagation velocity (e.g., shear wave velocity).

A = Cross-sectional area of rod.

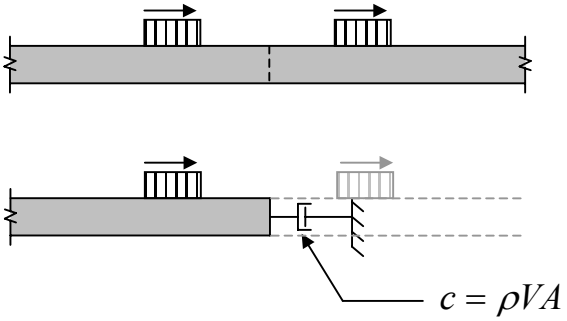

Figure 8-15. An infinitely long rod may be modeled using an appropriately selected damper.

Substituting Equation (8-14b) into Equation (8-29) and solving for V results in the following expression, referred to as Lysmer's velocity, V_{La}, (Holeyman 1985, Dobry and Gazetas 1986).

$$V_{La} = \frac{3.4}{1-\nu} \cdot r^2 \cdot \sqrt{\frac{G\gamma_t}{g}} \cdot \frac{1}{\rho A} = V_s \frac{3.4}{\pi(1-\nu)} \tag{8-30}$$

The modulus corresponding to V_{La} is:

$$
\begin{aligned}
E_{La} &= V_{La}^2 \cdot \rho \\
&= V_s^2 \cdot \left[\frac{3.4}{\pi(1-\nu)} \right]^2 \cdot \rho \\
&= G \cdot \left[\frac{3.4}{\pi(1-\nu)} \right]^2
\end{aligned}
\tag{8-31}
$$

Comparisons of E_{La} with E_y and E_c are shown in Figure 8-14.

Substitution of the above expression for E_{La} into Equation (8-26) results in an expression for maximum deviatoric shear strain:

$$
\gamma_{dev\,\max} = 0.85 \cdot (1-\nu)^2 (1+\nu) \frac{W a_{\max}}{g B^2 G}
\tag{8-32}
$$

where:
- $\gamma_{dev\,\max}$ = Maximum deviatoric shear strain.
- ν = Poisson's ratio.
- W = Weight of tamper.
- $a_{\max}$ = Peak acceleration.
- g = Acceleration due to gravity.
- B = Length of square contact area of tamper and soil.
- G = Shear modulus.

The above expression is solved iteratively using the shear modulus degradation curve for the soil, similar to the procedure shown in Figure 8-2. As throughout this thesis, the Ishibashi and Zhang (1993) shear modulus degradation curves, given previously as Equation (2-16), are recommended for use. These curves are functions of the plasticity index (I_p) of the soil and the effective confining pressure. For cohessionless soil, $I_p = 0$. The confining pressure is assumed to be that of a depth of about 10*ft*. This depth is selected to be below the depth of the impact crater and is judged to represent the soil most directly influencing the response of the tamper.

The final parameter that needs to be discussed is Poisson's ratio (ν), which was defined previously by Equation (8-25). From the theory of elasticity it can be shown that

Poisson's ratio can range from -1 to 0.5, where 0.5 corresponds to an incompressible material. Few materials have negative Poisson's ratios, with typical values ranging from 0 to 0.5 (Davis and Selvadurai 1996). For saturated soils subjected to rapid loading, the range is typically smaller, with the lower bound being greater than zero, depending on the drainage conditions, and the upper bound remaining 0.5. Laboratory experience has shown that it is difficult to determine reliable values of Poisson's ratio directly from experiments. Accordingly, Poisson's ratio is often determined indirectly from other parameters, which can readily and reliably be determined from field and/or laboratory tests. Several relations relating Poisson's ratio and other common parameters are:

$$\nu = \frac{M - 2G}{2(M - G)} \tag{8-33a}$$

$$\nu = \frac{3K - M}{3K + M} \tag{8-33b}$$

$$\nu = \frac{3K - 2G}{2(3K + G)} \tag{8-33c}$$

$$\nu = \frac{1 - 2\left(\frac{v_s}{v_p}\right)^2}{2\left[1 - \left(\frac{v_s}{v_p}\right)^2\right]} \tag{8-33d}$$

where: ν = Poisson's ratio.

M = Constrained modulus.

G = Shear modulus.

K = Bulk modulus.

v_s = Shear wave velocity.

v_p = P-wave velocity.

To assess Equation (8-20) and the proposed procedure for determining the degraded shear modulus, a comparison is made between predicted and recorded acceleration time

histories. The recorded time histories are those presented in Mayne and Jones (1983) for a 20.9*tonnes* tamper ($B = 1.9m$) dropped from 18.3*m* on to coal mine spoil, having $\nu =$ 0.37. The recorded and predicted time histories are shown in Figure 8-16. As may be observed in this figure, the computed time history using the degraded soil properties gives a very reasonable approximation of the recorded time histories, both in peak amplitude and period, especially given the gross simplifying assumptions made. To highlight the influence of soil non-linearity, a time history was computed using the small strain shear modulus, which is also shown Figure 8-16. This time history is significantly greater in amplitude and shorter in period than the recorded time histories.

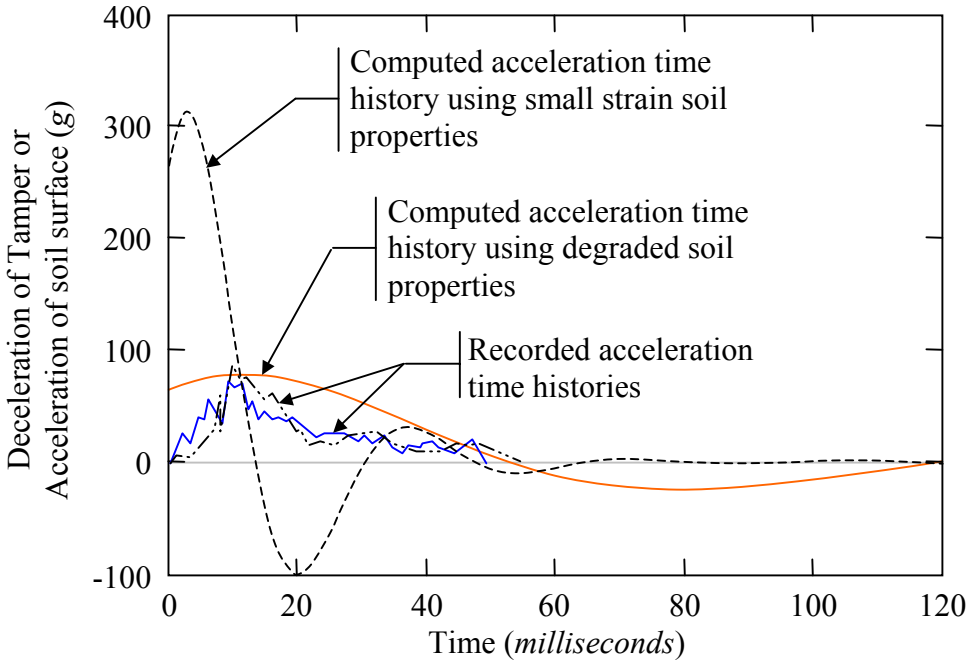

Figure 8-16. A comparison of computed and recorded acceleration time histories. The recorded time histories are from Mayne and Jones (1983).

Mayne and Jones (1983) also present peak acceleration values as a function of the drop height of the tamper. A comparison of this data with predicted peak accelerations is shown in Figure 8-17. As may be observed from this figure, the predicted accelerations are in reasonable agreement with the field observations.

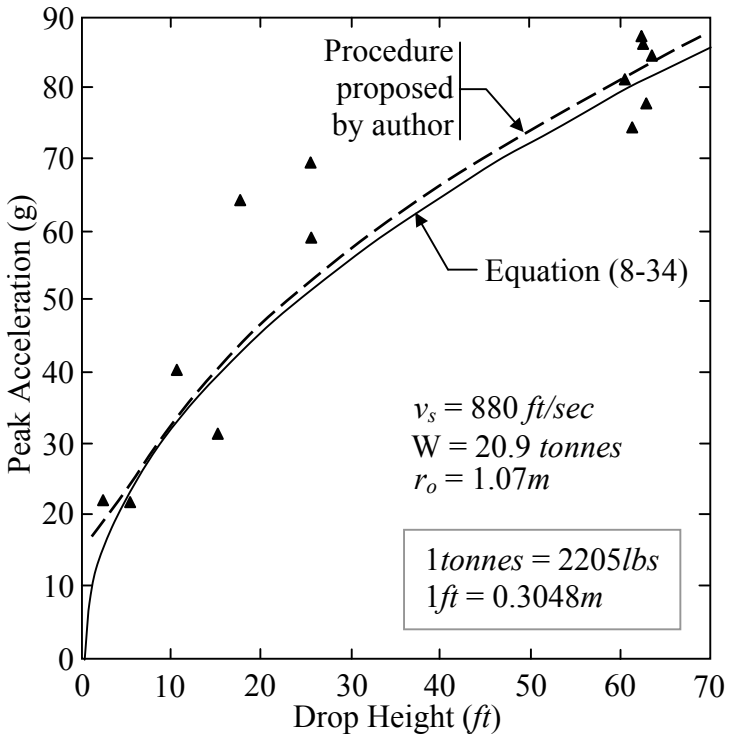

Figure 8-17. Predicted and measured peak acceleration values as a function of drop height of the tamper. (Measured data from Mayne and Jones 1983).

Alternative to the procedure developed by the author, Mayne and Jones (1983) proposed the following expression for estimating peak acceleration.

$$\frac{a_{\max}}{g} = v_{s\max} \cdot \sqrt{\frac{HB}{W}} \tag{8-34}$$

where: $a_{\max}$ = Peak acceleration of the soil surface.

W = Weight of tamper (*lbs*).

H = Drop height (*ft*).

B = Dimension of tamper (*ft*).

$v_{s\max}$ = Small strain shear wave velocity of the soil (*ft/sec*).

g = Acceleration due to gravity.

Although all are not explicitly stated in Mayne and Jones (1983), the following assumptions are inherent in the above expression:

Triangular shaped acceleration time history.

No participation of soil mass.

G = $0.1 \cdot G_{max}$
(based on field observations made by Hansbo 1977, 1978).

ν = 0.37

γ_t = $110 lb/ft^3$

k = $\frac{4Gr}{1-\nu}$

All of these assumptions are reasonable, and Equation (8-34) gives results very similar to those computed using the author's model (as shown in Figure 8-17), with much less computational effort. Accordingly, unless the field conditions deviate considerably from the above stated assumptions or unless the entire acceleration time history is required, the expression proposed by Mayne and Jones (1983) is recommended for use.

8.4.2 Response of the Soil at Depth for Deep Dynamic Compaction

The relationship between the maximum impact force on the soil surface and the maximum normal stress induced at depth in the profile is assumed to be:

$$\sigma_{max}(z) = \frac{F_{max}}{(B+z)^2} \tag{8-35}$$

where: $\sigma_{max}(z)$ = Maximum induced normal stress at depth z in the profile.

F_{max} = Maximum induced force on the surface of the profile.

B = Dimension of tamper.

z = Depth in the profile at which stress is being computed.

This expression inherently assumes a 2:1 stress distribution with depth, which is commonly assumed in static foundation design and was assumed in the deep dynamic compaction models proposed by Pearce and Scott (1975) and Mayne and Jones (1983).

The relationship between axial stress and axial strain given previously as Equation (8-23b) applies equally to the soils at the surface as to the soils at depth for the assumed truncated cone model. However, the soil modulus (E') will likely vary with depth. As discussed in the previous section, at the surface E' assumed is equal to E_{La}. However, as

the stresses spread with depth in the profile, a condition is eventually reached where the lateral strain is approximately zero for the soils directly beneath the tamper. At this depth, *E'* is equal to the constrained modulus (E_c). Such a variation of *E'* is only required because a one-dimensional cone model is being used to represent a three-dimensional process. If a full three-dimensional model is developed, the imposed stress conditions account for the variation in the apparent soil stiffness. Based on a limited parameter study conducted by the author, *E'* is assumed to vary parabolically from E_{La} at a depth of 10*ft* to E_c at a depth of 40*ft*. Above a depth of 10*ft*, *E'* is assumed equal to E_{La}. Although a more detailed study, both numerical and experimental, is required to confirm this assumption, the assumed variation of *E'* does not greatly influence the soil response for $0 \leq \nu \leq 0.4$. It is noted that both Holeyman (1985) and Wolf (1994) use variants of the truncated cone model proposed by the author. However, both assume *E'* is constant with depth: Holeyman (1985) assumed $E' = E_{La}$ and Wolf (1994) assumed $E' = E_c$, which are the lower and upper bounds assumed by the author.

The spreading of the stress front and the variation of the soil modulus (*E'*) are conceptually illustrated in Figure 8-18.

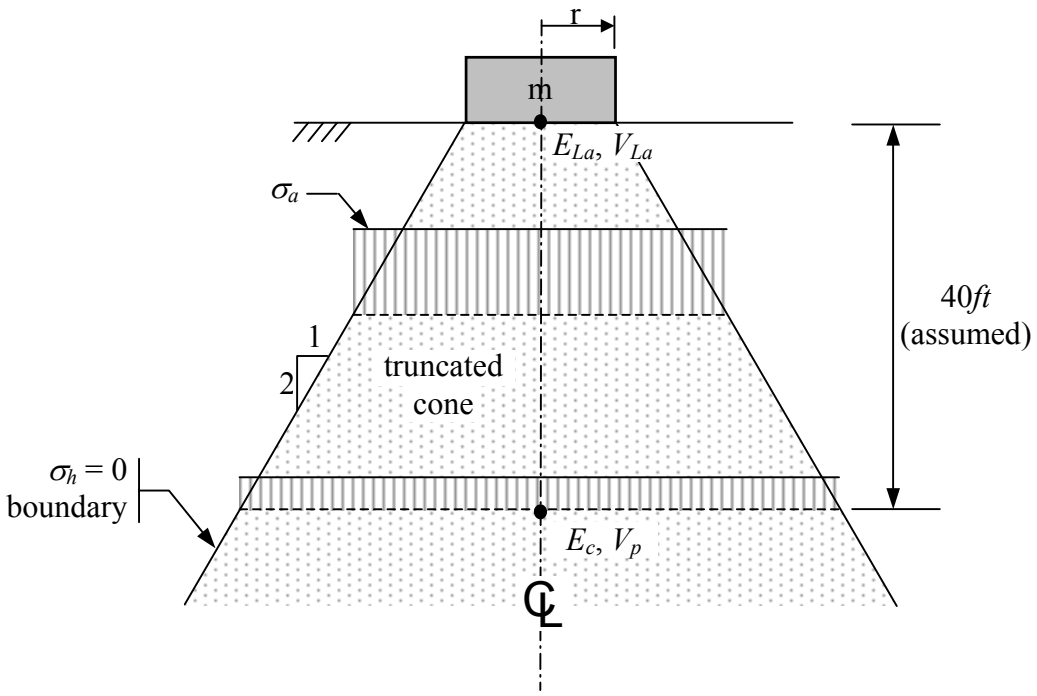

Figure 8-18. Truncated cone used to model induced stresses from impacting tamper on the surface of a profile. The soil modulus is assumed to vary parabolically from E_{La} at a depth of 10*ft* to E_c at a depth of 40*ft*, as shown in Figure 8-19b. Above a depth of 10*ft*, the soil modulus is assumed equal to E_{La}.

The following expression defines the parabolically varying *E'* as a function of depth (*z*).

$$E'(z) = V(z)^2 \cdot \frac{\gamma_t}{g} \tag{8-36a}$$

where: $E'(z)$ = Soil Modulus at depth z in the profile.

$V(z)$ = Propagation velocity of compression-extension wave at depth z in the profile.

$$= \begin{cases} V_{La} & for \quad z < z_1 \\ (V_p - V_{La}) \cdot \sqrt{\dfrac{z - z_1}{z_2 - z_1}} + V_{La} & for \quad z_1 \le z \le z_2 \\ V_p & for \quad z > z_2 \end{cases} \tag{8-36b}$$

z_1 = $10ft$ assumed.

z_2 = $40ft$ assumed.

z = Depth in the profile.

γ_t = Total unit weight of the soil.

g = Acceleration due to gravity.

Plots of both $V(z)$ and $E'(z)$ (i.e., Equations (8-36b) and (8-36a), respectively) are shown in Figure 8-19 for $\nu = 0.37$ and $v_s = 880\ ft/sec$.

In addition to E' and V varying as a result of the changing boundary conditions with depth, the relationship between axial and lateral strain is also assumed to vary as a result of the changing stress conditions. This can be understood from examining Figure 8-13, where at depths when $E' = E_c$, the ratio $\varepsilon_h/\varepsilon_a = 0$. This variation in the ratio $\varepsilon_h/\varepsilon_a$ is accounted for by the parameter C. From substitution of Equation (8-25) into Equation (8-24), the deviatoric shear strain is given by the following expression.

$$\gamma_{dev} = (1+\nu)\varepsilon_a$$
$$= C \cdot \varepsilon_a \qquad (8\text{-}37)$$

where: γ_{dev} = Deviatoric shear strain.

ν = Poisson's ratio.

ε_a = Axial strain.

C = Constant of proportionality relating deviatoric and axial strain.

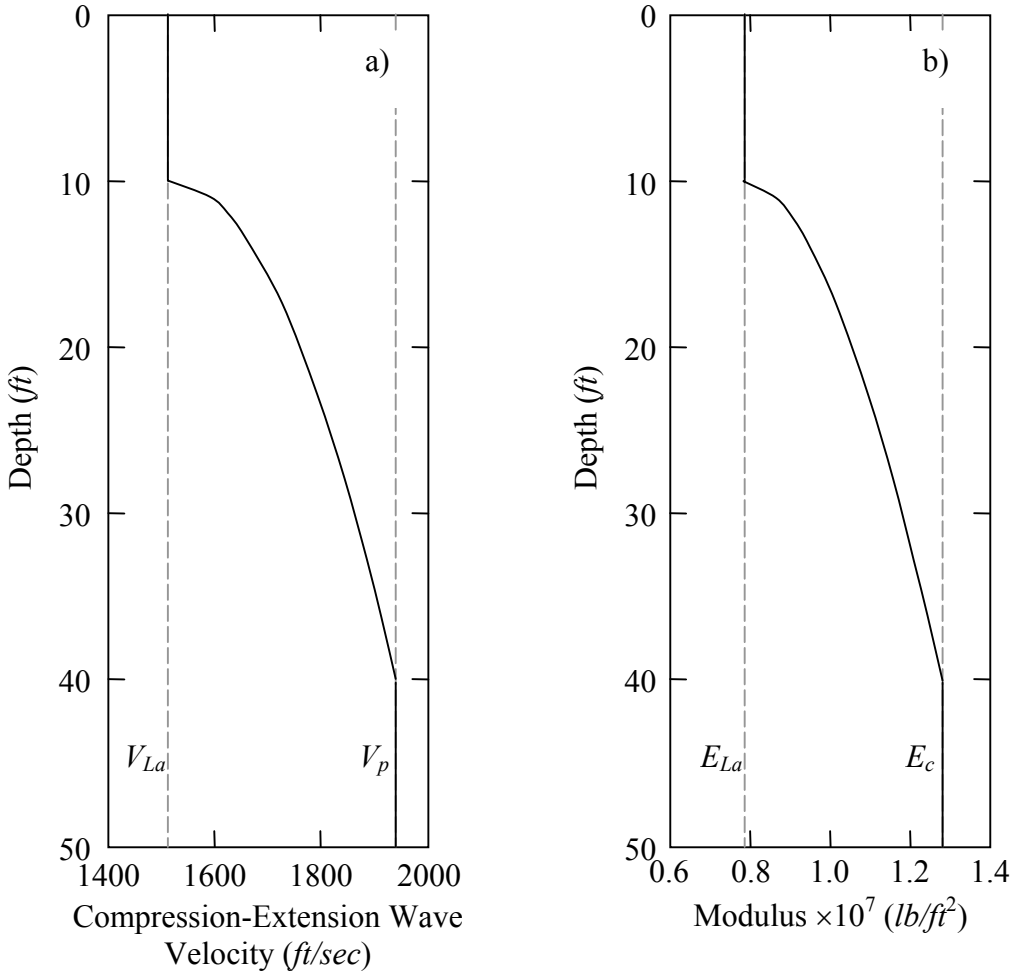

Figure 8-19. Variation of: a) propagation velocity of a compression-extension wave, and b) soil modulus, as a function of depth in the profile.

In Equation (8-37), the term $(1+\nu)$ is replaced by the constant of proportionality C, which is assumed to range from $(1+\nu) \le C \le 1$ to account for the variation of the ratio of $\varepsilon_h/\varepsilon_a$. Assuming a linear variation of C with E' results in the following expression.

$$C(z) = 1 + \frac{\nu}{E_{La} - E_c} \cdot E'(z) - \frac{E_c \nu}{E_{La} - E_c} \tag{8-38}$$

A plot of Equation (8-38) is shown in Figure 8-20. As with the assumed relationships expressing the variation of E' and V with depth, both numerical and experimental studies are required to verify Equation (8-38). However, from the limited parameter study

conducted by the author, the soil response is not greatly influenced by the assumed variation of the ratio $\varepsilon_h/\varepsilon_a$ for $0 \leq \nu \leq 0.4$.

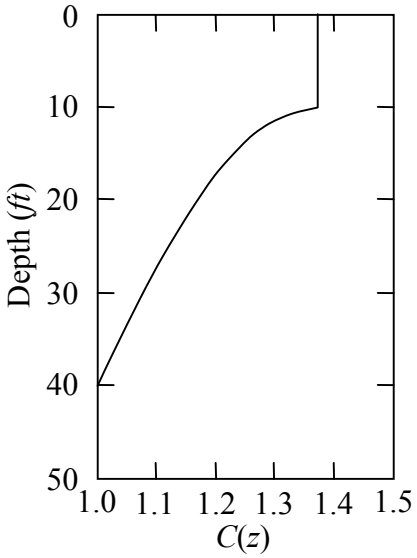

Figure 8-20. Variation of the constant of proportionality relating deviatoric and axial strains as a function of depth.

Finally, through a series of substitutions and algebraic manipulations, the deviatoric shear strain is given by the following expression.

$$\gamma_{dev}(z) = \frac{C(z)}{E'(z)} \cdot \frac{v_{s\max}\sqrt{HBW}}{(B+z)^2} \tag{8-39}$$

where:
- $\gamma_{dev}(z)$ = Deviatoric shear strain at depth z (*dimensionless*).
- $E'(z)$ = Soil modulus at depth z (Equation (8-36a)) (*lbs/ft*^{2}).
- $C(z)$ = Constant of proportionality relating deviatoric and axial strain (Equation (8-38)) (*dimensionless*).
- W = Weight of tamper (*lbs*).
- H = Drop height (*ft*).
- B = Dimension of tamper (*ft*).
- z = Depth in the profile at which stress is being computed (*ft*).
- $v_{s\max}$ = Small strain shear wave velocity of the soil (*ft/sec*).

Inherent to Equation (8-39) are all the assumptions listed for Equation (8-34), for the expressions $E'(z)$ and $C(z)$, and the assumption of a uniform stress distribution across the contact area between the tamper and soil. From a limited parameter study conducted by the author, none of the imposed assumptions strongly influence the computed results, and all the assumptions are reasonable to a first order approximation.

To account for soil non-linearity, the soil modulus, $E'(z)$, is assumed to vary as a function of the induced deviatoric shear strain. Employing the equivalent linear approach, Equation (8-39) is solved iteratively using the shear modulus degradation curve corresponding to each depth of interest. The general axial stress-strain behavior of soil subjected to impact loading is shown in Figure 8-21 (Scott and Pearce 1975 and Sinitsin 1983). As shown in this figure, at high levels of axial strain the soil strain hardens. The author found, quite serendipitously, that strain hardening could be approximately modeled by slightly modifying the Ishibashi and Zhang (1993) shear modulus degradation curves. The modification entails simply assuming that the shear modulus ratio remains constant above a designated level of shear strain. This is shown in Figure 8-22a, wherein the shear modulus ratio is assumed constant for shear strains above 1%. The resulting axial stress-strain curve is shown in Figure 8-22b. For comparison purposes, the commonly used hyperbolic stress-strain relation is also shown in Figure 8-22b.

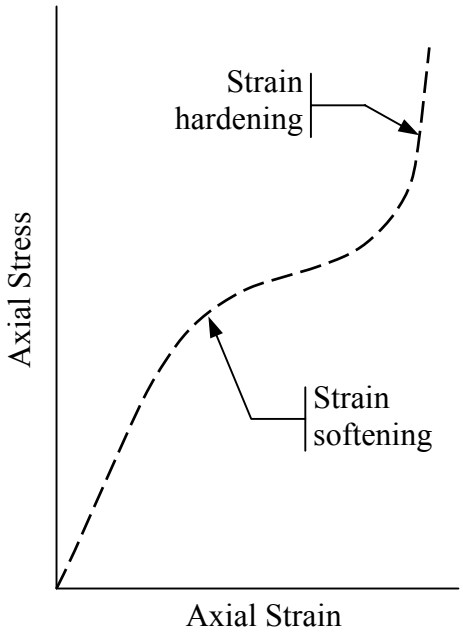

Figure 8-21. General axial stress-strain behavior of soil subjected to impact loading. (Adapted from Scott and Pearce 1975).

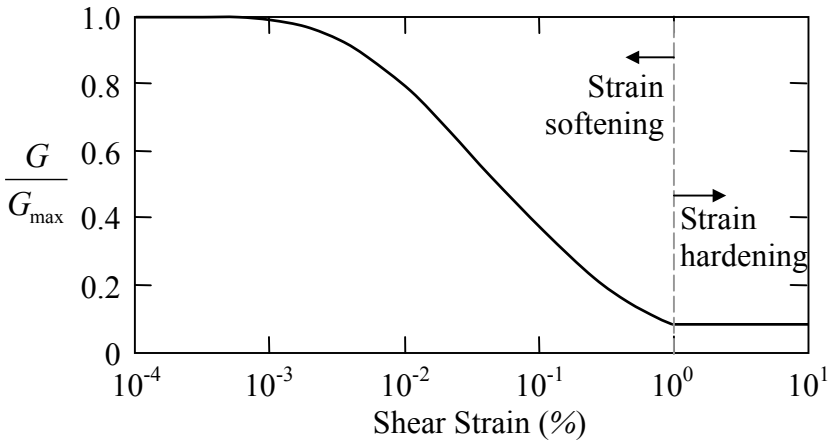

Figure 8-22a. Modified shear modulus degradation curve to incorporate strain hardening effects.

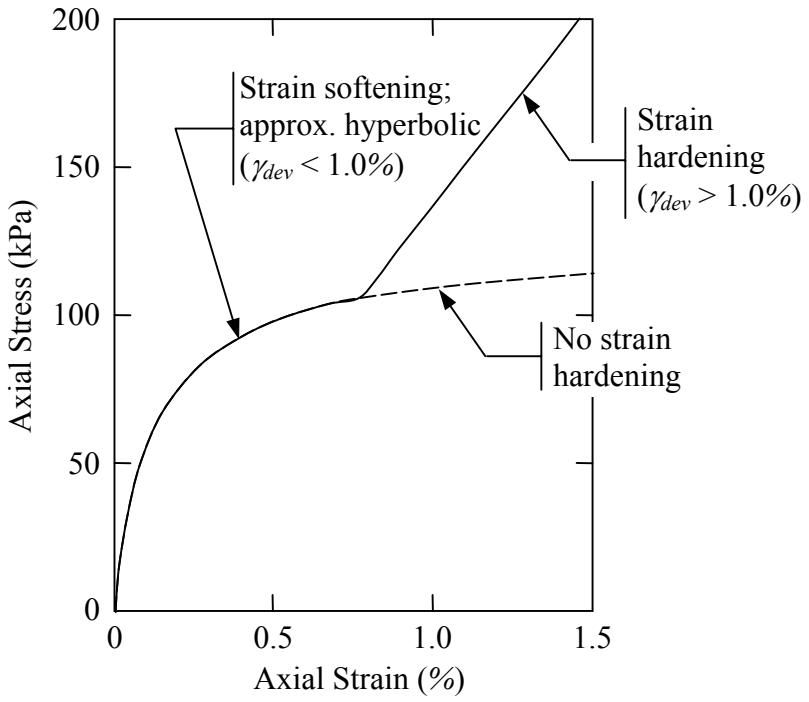

Figure 8-22b. Axial stress-strain relation corresponding to modified Ishibashi and Zhang shear modulus degradation curve shown in Figure 8-22a. For comparison, the commonly used hyperbolic stress-strain relation is shown, which does not account for strain hardening effects.

Once the induced deviator shear strain is known as a function of depth in the soil profile, the normalized dissipated energy can be estimated using the following expression.

$$NED = 2\pi D_\gamma G_{\max} \left(\frac{G}{G_{\max}} \right)_\gamma \gamma_{dev}^2 \frac{N_{eqv}}{\sigma'_{mo}} \tag{8-40}$$

where: NED = Normalized energy demand (Section 5.2.3).

D_γ = Damping ratio (Section 3.3.2; Equation (3-4)).

G_{max} = Small strain shear modulus (Section 2.2.2; Equation (2-12)).

$G/G_{\max}$ = Shear modulus ratio (Equation (2-16)).

γ_{dev} = Deviatoric shear strain (Equation (8-39)).

N_{eqv} = Number of equivalent cycles of loading.

σ'_{mo} = Initial mean effective confining stress (Section 2.2.2; Equation (2-13)).

Following the approach outlined in Chapter 5 (Section 5.2.3), acceleration time histories computed using Equation (8-20) were analyzed, and it was determined that N_{eqv} is approximately 0.75 cycles.

Using the above expression for *NED* in conjunction with the expression for the normalized energy capacity of the soil (*NEC*: Equation (5-11), Figure 5-11), the depth of induced liquefaction was estimated for the case where a 20.9*tonnes* tamper is dropped 18.3*m* onto the surface of a clean sand profile having a constant $N_{1,60}$ = 5*blws/ft* and the groundwater table at 10*ft* below the soil surface. The results of these calculations are shown in Figure 8-23 for three different values of Poisson's ratio: 0.2, 0.37, and 0.495, wherein liquefaction is predicted at depths where *NED* > *NEC*. As shown in this figure, the maximum depth of predicted liquefaction decreases as the assumed value of Poisson's ratio increases. In line with the values assumed by Mayne and Jones (1983) and Pan and Selby (2000) in modeling deep dynamic compaction, a Poisson's ratio of around 0.35 is likely appropriate. Finally, the kinks in the *NED* curves result from the modifications made to the Ishibashi and Zhang shear modulus degradation curves to account for strain hardening effects (i.e., at depths shallower than the kinks, $\gamma_{dev} \geq 1.0\%$).

Also shown in Figure 8-23 are the maximum depths of improvement computed using the empirical expression presented in Chapter 7 (i.e., Equation (7-6)) for three different *n* values: 0.3, 0.5, and 0.8. Assuming $n = 0.5$ and $\nu = 0.37$, the maximum depth of improvement predicted using the empirical expression is in reasonable agreement with the maximum depth of liquefaction predicted using the proposed first order model. A closer agreement between the two predicted depths is realized if it is considered that densification will occur slightly beyond the maximum depth of induce liquefaction.

Although the favorable comparison between the predicted depths of improvement and induced liquefaction lend credence to the validity of the proposed numerical model, additional parameter studies are required to more fully evaluate the model and the inherent assumptions used in its development.

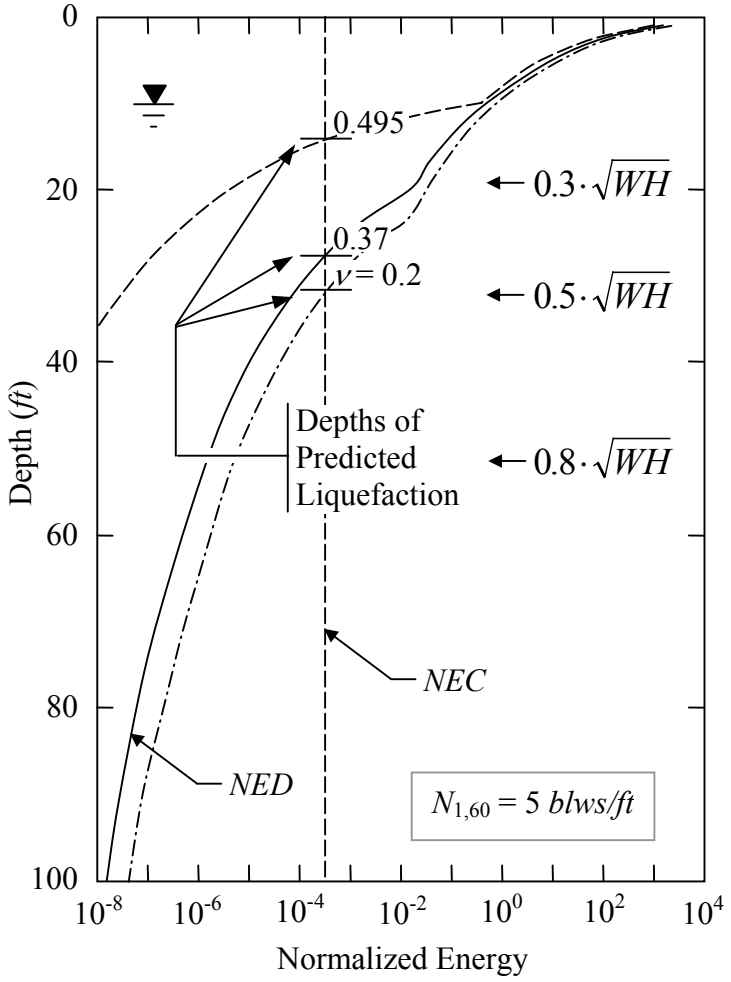

Figure 8-23. Comparison of the predicted depth of induced liquefaction using the numerical model proposed by the author to the predicted depth of improvement using empirical expressions.

8.5 Numerical Modeling of Explosive Compaction

The proposed model for explosive compaction is based on cavity expansion theory and is similar to the vibro-compaction model in that both use empirical attenuation relations in computing *NED*. Also, the proposed model for explosive compaction is similar to the deep dynamic compaction model in that the iterative solution for the degraded soil properties is based on the induced deviatoric shear strain. As discussed in Chapter 7 (Section 7.4.1), several mechanisms lead to the breakdown of the soil structure during blasting. However, the proposed first order model inherently assumes that the high

intensity shockwave is the dominant mechanism, which is similar to the inherent assumption in the higher order model proposed by Wu (1995, 1996).

The governing differential equation for the dynamic response of a homogeneous, isotropic, elastic whole-space surrounding a spherical cavity is given by the following expression (Sharpe 1942).

$$(\lambda + 2G) \cdot \left(\frac{\partial^2 \phi}{\partial R^2} + \frac{2}{R} \frac{\partial \phi}{\partial R} \right) = \rho \frac{\partial^2 \phi}{\partial t^2} \tag{8-41}$$

where: λ = Lame's parameter.

G = Shear modulus of wholespace.

ϕ = Displacement potential, discussed below.

ρ = Mass density of the whole space.

R = Radial distance from the center of the charge.

t = Time.

Sharpe (1942) derived a solution for the above differential equation for a pressure function of the form $p = P_o \cdot e^{-\alpha' t}$ acting on the wall of a spherical cavity of radius a in a wholespace having a Poisson's ratio (ν) equal to 0.25. Wu (1995) generalized Sharpe's solution for wholespaces having different ν, this generalize solution is:

$$\phi(T) = \frac{P_o a}{R\rho[\omega_o^2 + (\alpha_o - \alpha')^2]} \cdot \left\{ e^{-\alpha_o T} \cdot \left[\cos(\omega_o T) + \frac{\alpha_o - \alpha'}{\omega_o} \sin(\omega_o T) \right] - e^{-\alpha' T} \right\} \tag{8-42}$$

where: $\phi(T)$ = Displacement potential as a function of T.

$$\alpha_o = \frac{v_p \cdot (1 - 2\nu)}{a \cdot (1 - \nu)}$$

$$\omega_o = \frac{v_p \cdot (1 - 2\nu)^{0.5}}{a \cdot (1 - \nu)}$$

$$T = t - \frac{(R - a)}{v_p}$$

v_p = P-wave velocity.

a = Radius of spherical charge/cavity.

ν = Poisson's ratio.

R = Radial distance from the center of the charge.

t = Time.

α' = Decay parameter of load.

ρ = Mass density of the whole space.

P_o = Amplitude of pressure at $R = a$ and $t = 0$.

The radial displacement in the wholespace (u_R) is related to the displacement potential by:

$$u_R(T) = \frac{\partial \phi(T)}{\partial R} \qquad \text{(Sharpe 1942)} \tag{8-43a}$$

Differentiating Equation (8-42) with respect to R, gives:

$$u_R(T) = \begin{cases} 0 & \text{for } T < 0 \\ \dfrac{P_o a}{R^2 \rho \cdot [\omega_o^2 + (\alpha_o + \alpha')^2]} \cdot & \\ \left\langle -\left\{ e^{-\alpha_o T}\left[\cos(\omega_o T) + \dfrac{\alpha_o + \alpha'}{\omega_o} \sin(\omega_o T) \right] \right. \right. & \\ \left. - e^{-\alpha' T} \right\} + \dfrac{R}{v_p} \cdot \left\{ e^{-\alpha_o T}\left[\alpha' \cos(\omega_o T) \right. \right. & \\ \left. \left. + \dfrac{\omega_o^2 + \alpha_o^2 - \alpha_o \alpha'}{\omega_o} \sin(\omega_o T) \right] - \alpha' e^{-\alpha' T} \right\} \Big\rangle & \text{for } T \geq 0 \end{cases} \tag{8-43b}$$

Similarly, the radial velocity in the wholespace ($\dot{u}_R$) is related to the displacement potential by:

$$\begin{aligned} \dot{u}_R(T) &= \frac{\partial^2 \phi}{\partial R \partial t} \\ &= \frac{\partial u_R}{\partial t} \end{aligned} \tag{8-44a}$$

Differentiating Equation (8-43b) with respect to t, gives:

$$\dot{u}_R(T) = \begin{cases} 0 & \text{for } T < 0 \\ \dfrac{P_o a}{R^2 \rho \cdot [\omega_o^2 + (\alpha_o + \alpha')^2]} \cdot & \\ \left\langle \left\{ e^{-\alpha_o T} \left[\alpha' \cos(\omega_o T) + \dfrac{\omega_o^2 + \alpha_o^2 - \alpha_o \alpha'}{\omega_o} \sin(\omega_o T) \right] \right. \right. & \\ \left. - \alpha' e^{-\alpha' T} \right\} + \dfrac{R}{v_p} \cdot \left\{ e^{-\alpha_o T} \left[(\omega_o^2 + \alpha_o^2 - 2\alpha_o \alpha') \cos(\omega_o T) \right. \right. & \text{for } T \geq 0 \\ \left. \left. - \dfrac{\alpha_o \omega_o^2 + \alpha' \omega_o^2 + \alpha_o^3 - \alpha' \alpha_o^2}{\omega_o} \sin(\omega_o T) \right] + \alpha'^2 \, e^{-\alpha' T} \right\} \Big\rangle & \end{cases} \tag{8-44b}$$

From cavity expansion theory, the deviatoric shear strain induced in the wholespace is given by the following expression.

$$\gamma_{dev} = \frac{1}{2} \cdot [\varepsilon_{rr} - \varepsilon_{\theta\theta}] \qquad \text{(e.g., Hryciw 1986)} \tag{8-45a}$$

where: γ_{dev} = Deviatoric shear strain.

ε_{rr} = Radial strain.

$$= \frac{\partial^2 \phi}{\partial r^2} = \frac{\dot{u}_R}{v_p}$$

$\varepsilon_{\theta\theta}$ = Tangential strain.

$$= \frac{1}{r} \frac{\partial \phi}{\partial r} = \frac{u_R}{r}$$

In alternate form, the above expression may be written:

$$\gamma_{dev} = \frac{1}{2} \cdot \left[\frac{\dot{u}_R}{v_p} + \frac{u_R}{R} \right] \tag{8-45b}$$

The relative contributions of the terms inside the brackets of the above expression (i.e., ε_{rr} and $\varepsilon_{\theta\theta}$) can be examined using Equations (8-43b) and (8-44b). The time histories for ε_{rr} and $\varepsilon_{\theta\theta}$ are shown in Figure 8-24 at two distances from the center of the charge (R) for a wholespace having $v_s = 150 m/sec$ and $v_p = 281 m/sec$ (i.e., $\nu = 0.3$). As may be

observed from this figure, as R increases, the relative contribution of $\varepsilon_{\theta\theta}$ (= u_R/R) rapidly decreases (i.e., $\varepsilon_{\theta\theta} \approx 0$ at $R = 1.0m$). Accordingly, the deviatoric shear strain can be reasonably approximated as:

$$\gamma_{dev} \approx \frac{1}{2}\frac{\dot{u}_R}{v_p} \tag{8-45c}$$

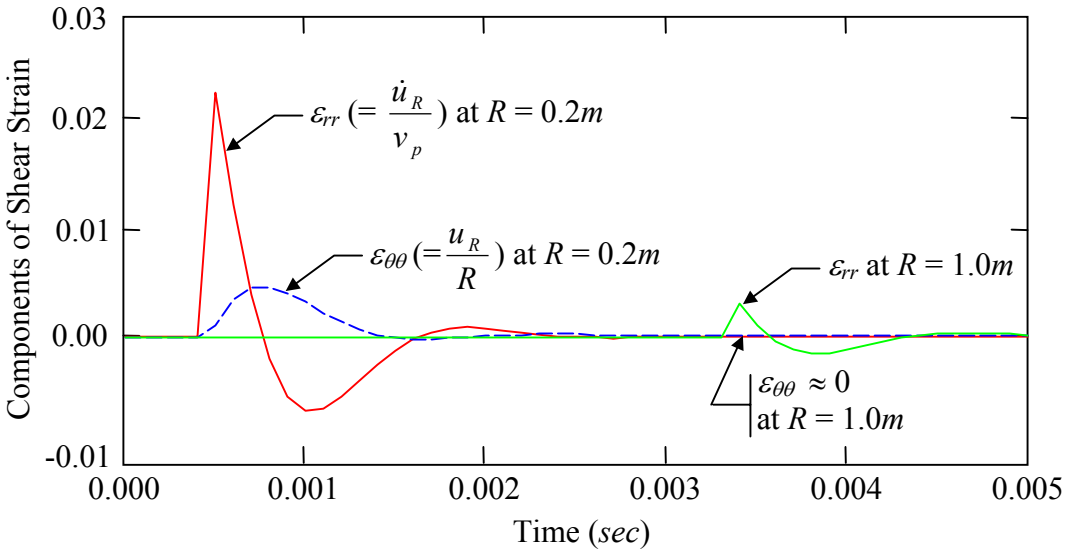

Figure 8-24. Relative contribution of the ε_{rr} and $\varepsilon_{\theta\theta}$ as for two distances from the cavity wall.

As with the proposed model for deep dynamic compaction, the deviatoric shear strain is used in conjunction with the shear modulus degradation curves to iteratively determine the degraded soil properties. However, the assumptions inherent to Equations (8-44b) for radial velocity do not apply to actual soil profiles (i.e., homogeneous, isotropic, elastic wholespace). As a result, empirical attenuation relations for radial velocity are used. Many blast attenuation relations have the form:

$$\dot{u}_{peak} = C_1 \cdot \left(\frac{R}{W^m}\right)^{-n} \tag{8-46}$$

where: $\dot{u}_{peak}$ = Peak particle velocity at distance R from the center of the charge (*m/sec*).

R = Radial distance from the center of the charge (*m*).

W = Weight of the charge (kg).

m = Constant that is a function of the geometry of the charge.

C_1 = Empirically determined constant.

n = Empirically determined constant.

Values for m, C_1, and n from various studies are listed in Table 8-3, and the relations listed for deep, concentrated charges are plotted in Figure 8-25. As may be observed from this figure, a great deal of scatter exists among the various relations.

Table 8-3. Coefficients for blast attenuation expression. (Adapted from Narin van Court and Mitchell 1994b).

Test Type	C_1	m	n	Reference
Deep blasting, Columnar charges	0.6	1/2	1.35	Long et al. (1981)
	11.6	1/2	1.67	Duvall et al. (1967)
	7.2	1/2	1.15	Sanders (1982)
	1.1 to 3.6	1/2	1.15	Charlie (1985)
Deep blasting, Concentrated charges	12	1/3	1.50	Charlie et al. (1985a)
	5.6	1/3	1.50	Drake and Little (1983)
	8.75	1/3	2.06	Charlie et al. (1992)
	8.0	1/3	2.30	Charlie et al. (1985b)
	1.1 to 3.6	1/3	2.30	Charlie (1985)
Underwater blasting, loose sand	11.9	1/3	1.45	Schure (1990)
	17.7	1/3	1.45	Schure (1990)
Underwater blasting, medium sand	16.6	1/3	1.45	Schure (1990)
	13.9	1/3	1.45	Schure (1990)
Underwater blasting, dense sand	12.8	1/3	1.5	Bretz (1989)

Besides the variability in site conditions and explosive types, some of the scatter shown in Figure 8-25 may be due to the specifics of the attenuation relations (e.g., location of the recorded motions, peak particle velocity being represented). Due to the complexities

of wave propagation in actual soil profiles, it is expected that the peak particle velocities recorded on the surface of the profile will differ from those recorded at depth. Also, the peak particle velocities represented by the relations in Table 8-3 are not necessarily the same. As discussed in Mayne (1985), attenuation relations commonly represent: the maximum peak velocity for any one of the three orthogonally-oriented components of motion; the square root of the sum of the squares of the peaks from each of the three orthogonally-oriented components of motion; or the true vector sum, which is the maximum of the square root of the sum of the squares the three orthogonally-oriented components at a given time *t*.

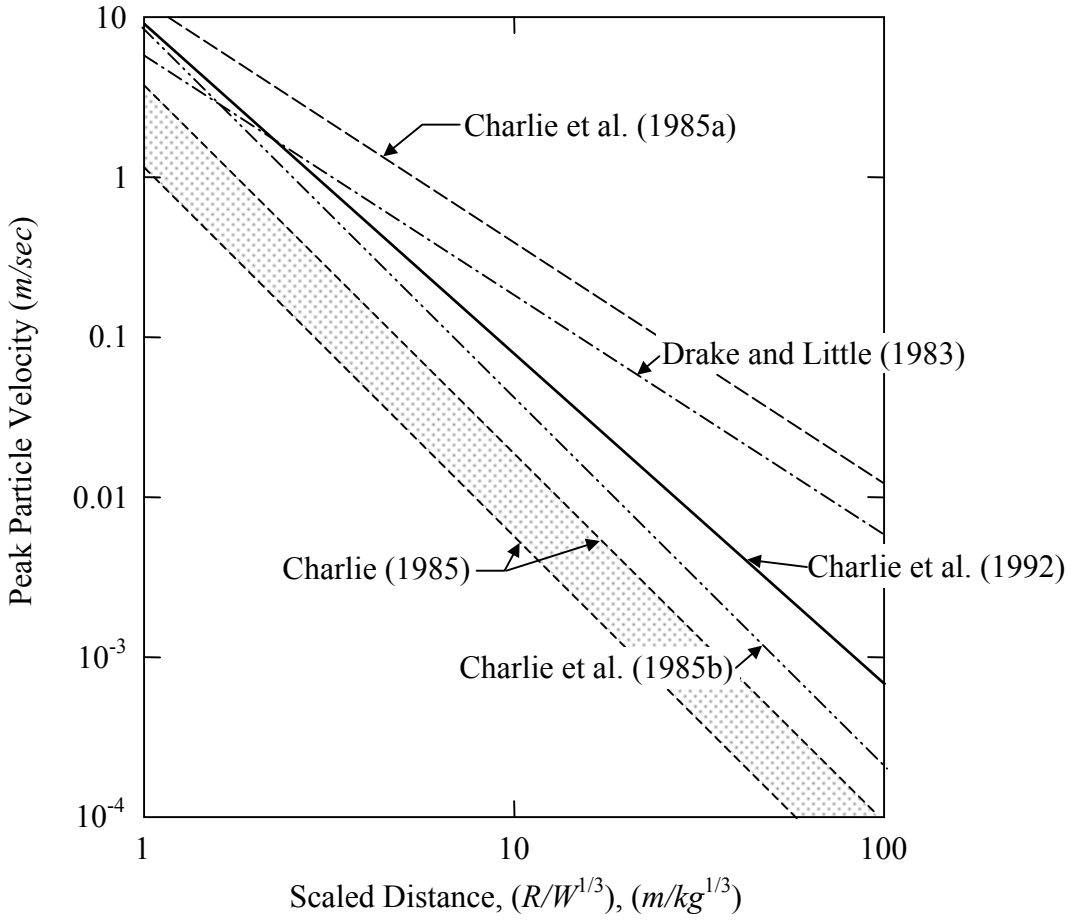

Figure 8-25. Empirical attenuation relations for deep, concentrated charges; refer to Table 8-3.

For computing the blast induced deviatoric shear strain using Equation (8-45c), the peak radial (or longitudinal) velocity measured at depth in the profile is needed. Unfortunately, the details of all the relations listed in Table 8-3 could not be ascertained by the author. As a first order approximation, the attenuation relation proposed by Charlie et al. (1992) is used. As may be observed from Figure 8-25, this relation lies in the middle of the range of relations listed in Table 8-3 for deep, concentrated charges.

The relationship between the P-wave velocity (v_p) for the degraded soil profile and the small strain shear wave velocity ($v_{s\,\max}$) is:

$$v_p = v_{s\,\max} \cdot \sqrt{\left(\frac{G}{G_{\max}}\right)_\gamma} \cdot \sqrt{\frac{2(1-\nu)}{1-2\nu}} \tag{8-47}$$

where: v_p = P-wave velocity for the degraded soil profile.

$v_{s\,\max}$ = Small strain shear wave velocity.

ν = Poisson's ratio.

$G/G_{\max}$ = Ratio of degraded to small strain shear moduli.

Substitution of the above equation into Equation (8-45c) results in the following expression for deviatoric shear strain in terms of the shear modulus ratio $G/G_{\max}$. Similar to the procedure outlined for deep dynamic compaction, this expression is solved iteratively using the modified Ishibashi and Zhang shear modulus degradation curves.

$$\gamma_{dev} \approx \frac{\dot{u}_{R\,peak}}{2 \cdot v_{s\,\max} \cdot \sqrt{\left(\frac{G}{G_{\max}}\right)_\gamma} \cdot \sqrt{\frac{2(1-\nu)}{1-2\nu}}} \tag{8-48}$$

Once the induced deviator shear strain is known, the normalized dissipated energy can be estimated using the following expression.

$$NED = 2\pi D_\gamma G_{\max} \left(\frac{G}{G_{\max}}\right)_\gamma \gamma_{dev}^2 \frac{N_{eqv}}{\sigma'_{mo}} \tag{8-49}$$

where: NED = Normalized energy demand (Section 5.2.3).

D_γ = Damping ratio (Section 3.3.2; Equation (3-4)).

G_{max} = Small strain shear modulus (Section 2.2.2; Equation (2-12)).

$G/G_{\max}$ = Shear modulus ratio (Equation (2-16)).

γ_{dev} = Deviatoric shear strain (Equation (8-48)).

N_{eqv} = Number of equivalent cycles of loading.

σ'_{mo} = Initial mean effective confining stress (Section 2.2.2; Equation (2-13)).

Following the approach outlined in Chapter 5 (Section 5.2.3), velocity time histories computed using Equation (8-44b) were analyzed, and it was determined that N_{eqv} is approximately 0.75 cycles, similar to N_{eqv} for deep dynamic compaction.

Using the above expression for *NED* in conjunction with the expression for the normalized energy capacity of the soil (*NEC*: Equation (5-11), Figure 5-11), the radial extent of induced liquefaction was estimated for 5.5*kg* charge detonated at 12*m* in a clean sand profile having a constant $N_{1,60}$ = 5*blws/ft* and the groundwater table at 3.05*m* (10*ft*) below the soil surface. The results of these calculations are shown in Figure 8-26 for three different values of Poisson's ratio: 0.2, 0.37, and 0.495, wherein liquefaction is predicted when *NED* > *NEC*. Similar to the trend noted for deep dynamic compaction, the radial extent of liquefaction decreases as the assumed value of Poisson's ratio increases.

Also shown in Figure 8-26 are the empirically determined ranges for the radial extent of improvement given by Kok (1981) and Ivanov (1967), which were previously presented in Chapter 7 (Section 7.4.2). Assuming a Poisson's ratio of 0.37, the radial extents of induced liquefaction and of ground improvement, predicted using the proposed numerical model and the empirical ranges given by Kok (1981) and Ivanov (1967), respectively, are in good agreement.

However, for blast loading of saturated sands, Poisson's ratio is likely to be closer to 0.495 than 0.37. For example, the author calculated the Poisson's ratio used in the numerical studies of Awad (1990) and Wu (1996) to be approximately 0.46 and 0.496, respectively. Awad's analyses under predicted the radial extent of induced liquefaction

by a factor of about two, similar to the author's model if 0.495 is assumed for Poisson's ratio. Although Wu's predictions were close to those observed in the field, Wu's model includes both a viscous damping term and a non-linear stress-strain relation. The inclusion of the viscous damping term provides an additional mechanism for energy dissipation beyond the hysteretic mechanism inherent to the non-linear soil behavior. Wu selected the damping coefficients such that the predicted results and field observations were in good agreement (i.e., Wu calibrated his model using existing data such that the model can be used for predicting future events). Although possibly not as fundamentally correct as Wu's approach, the energy dissipation in the author's proposed model can be achieved by using a lower Poisson's ratio than the soil parameters dictate (i.e., using $\nu =$ 0.37, as opposed to 0.495).

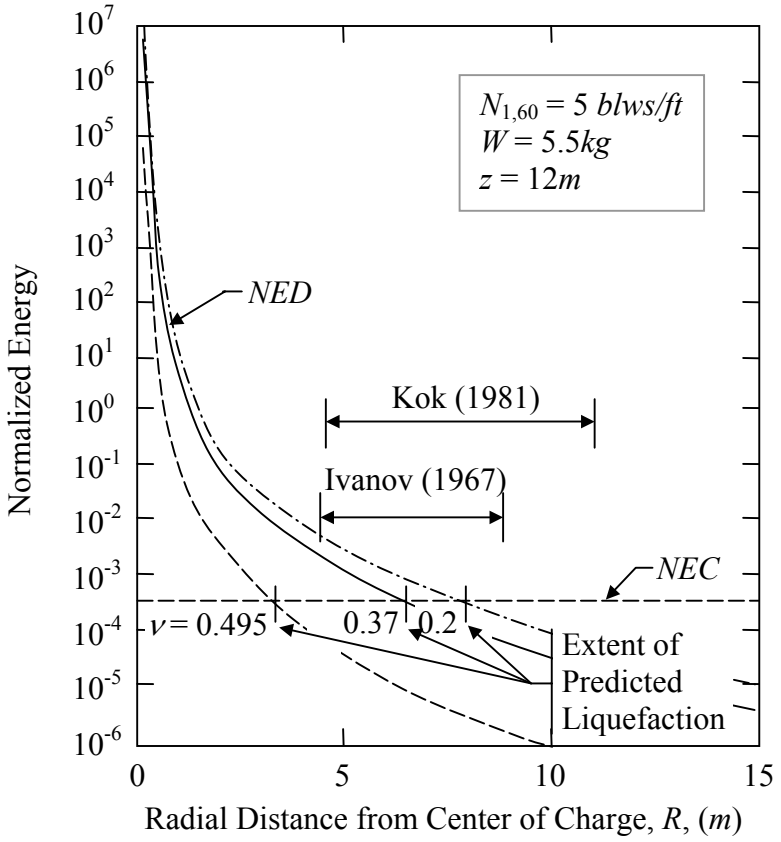

Figure 8-26. Comparison of the predicted radial extent of induced liquefaction using the numerical model proposed by the author to the predicted radial extent of improvement using empirical guidelines proposed by Ivanov (1967) and Kok (1981).

8.6 Higher Order Numerical Modeling for Remedial Ground Densification

As discussed in Section 8-2, the reconciliation of results computed using lower and higher order models, as well as favorable comparisons of computed results with field observations, is probably the best approach for verifying and validating numerical models. Alternatively to this approach, in this chapter, the results from proposed first order models were compared directly to empirical expressions and guidelines, without the benefit of comparisons with higher order model predictions. Accordingly, many of the assumptions inherent in the proposed first order models have not been fully validated.

In attempt to more fully evaluate the proposed first order models, the author developed both lumped mass and continuum higher order models to compute the spatial distribution of energy dissipation in the soil during treatment. However, the predictive capabilities of the models were limited, with the continuum model having the greatest potential for further development. Due to the assumptions inherent in the higher order models developed by the author (e.g., constitutive model, boundary conditions, source loading), the credibility given to the computed results was less than that given to the proposed first order models. Accordingly, the details of the models are not deemed necessary to report. However, Table 8-4 lists several higher order models for remedial ground densification techniques.

Table 8-4. Higher order models for remedial ground densification.

Ground Improvement Technique	Model Description	Reference
Vibro-compaction	• Non-linear model, specific details not known	Fellin (2000)
Deep Dynamic Compaction	• 1D-Lumped mass model • Single phase • Hyperbolic non-linear constitutive model	Holeyman (1985)
	• 2D-Finite element model • Single phase • Mohr-Coulomb elasto-plastic constitutive model	Pan and Selby (2000)
Explosive Compaction	• 3D-Lumped mass model • Single phase • von Mises elasto-plastic constitutive model	Ang (1966)*
	• 2D-Finite element model • Two phase, fully coupled pore pressure generation • Non-linear cap model	Awad (1990)
	• 1D-Finite element model • Single phase, uncoupled pore pressure generation • Hyperbolic non-linear constitutive model	Wu (1995, 1996)

*Originally developed for modeling blast wave propagation in soil.

8.7 Summary and Conclusions

The interactions between soil and remedial densification systems are very complex. However, based on a series of simplifying assumptions, first order models for the vibratory probe method, deep dynamic compaction, and explosive compaction are

proposed. All of the proposed models assume a single phase medium and use an iterative, equivalent linear type approach to account for soil non-linearity. Both the vibro-compaction and explosive compaction models use empirical attenuation relations to estimate the strain induced in the soil during treatment, while the deep dynamic compaction model assumes a 2:1 stress distribution with depth. Once the amplitude of the induced strain is known, the shear modulus and damping degradation curves are used to compute the energy dissipated in the soil as a function of distance from the source.

In comparing the model predictions with empirical guidelines for the vibratory probe method, the predicted lateral extent induced liquefaction is slightly less than empirical guidelines for the lateral extent of improvement. An inherent assumption was made in regards to the relation between peak and steady state amplitudes of vibrations, which in turn was used to compute the induced shear strain. However, the under-prediction of the extent of improvement is hypothesized to be related to improvement mechanisms and not due to the assumed attenuation relation. As discussed in Chapter 7, both increased density and increased lateral effective confining pressure contribute to the soil improvement. Accordingly, the lateral extent of improvement should extend beyond the zone of induced liquefaction.

In comparing model predictions with empirical expressions for deep dynamic compaction, the predicted depth of liquefaction is in reasonable agreement predicted depth of improvement computed using an empirical expression. One of the most influential model parameters is Poisson's ratio (ν), which inherently is a function of drainage conditions for the given load. The predicted depth of liquefaction decreases as ν increases. Based on the work of Mayne and Jones (1983) and Pan and Selby (2000), $\nu \approx 0.35$ is assumed to be reasonable and yields good results. However, further study is required to refine this estimated value.

In comparing model predictions with empirical guidelines for explosive compaction, the predicted radial extent of liquefaction for $\nu \approx 0.37$ is in reasonable agreement predicted radial extent of improvement per empirical guidelines. The assumed value of Poisson's

ratio (i.e., $\nu = 0.37$) is likely smaller than the soil properties, load rate, and drainage conditions dictate. However, use of a smaller than dictated Poisson's ratio appears to be a simple way to account for energy dissipation mechanisms not explicitly accounted for in the proposed model.

Based on the analyses and comparisons presented in this chapter and summarized above, the cumulative energy dissipated in a unit volume of soil, normalized by the initial mean effective confining stress, up to the point of initial liquefaction appears to be comparable for both earthquake type and remedial densification loadings. The implication being that the energy-based *Capacity* curve derived from earthquake case histories is applicable for use in remedial ground densification design. Additional research is required to verify and/or refine the proposed first order models and to develop design procedures for remedial ground densification programs that incorporate energy-based concepts. The ultimate goal being that such design procedures would lead to improved feasibility assessments of the various remediation techniques for given field conditions and improved initial designs over those that can be achieved by the currently used empirical expressions and guidelines.